Astronomy & Astrophysics

Comprehensive observations of the bright and energetic Type Iax SN 2012Z: Interpretation as a Chandrasekhar mass white dwarf explosion[⋆,⋆⋆,⋆⋆⋆]

M. D. Stritzinger[1], S. Valenti[2,3], P. Hoeflich[4], E. Baron[5,6], M. M. Phillips[7], F. Taddia[8], R. J. Foley[9], E. Y. Hsiao[1,7], S. W. Jha[10], C. McCully[10], V. Pandya[10], J. D. Simon[11], S. Benetti[12], P. J. Brown[13], C. R. Burns[11], A. Campillay[7], C. Contreras[1,7], F. Förster[14], S. Holmbo[1], G. H. Marion[15], N. Morrell[7], and G. Pignata[16]

[1] Department of Physics and Astronomy, Aarhus University, Ny Munkegade 120, 8000 Aarhus C, Denmark
e-mail: max@phys.au.dk
[2] Las Cumbres Observatory Global Telescope Network, Inc. Santa Barbara, CA 93117, USA
[3] Department of Physics, University of California, Santa Barbara, Broida Hall, Mail Code 9530, Santa Barbara, CA 93106-9530, USA
[4] Department of Physics, Florida State University, Tallahassee, FL 32306, USA
[5] Homer L. Dodge Department of Physics and Astronomy, University of Oklahoma, 440 W. Brooks, Rm 100, Norman, OK 73019-2061, USA
[6] Hamburger Sternwarte, Gojenbergsweg 112, 21029 Hamburg, Germany
[7] Carnegie Observatories, Las Campanas Observatory, Casilla 601 La Serena, Chile
[8] The Oskar Klein Centre, Department of Astronomy, Stockholm University, AlbaNova, 10691 Stockholm, Sweden
[9] Astronomy Department, University of Illinois at Urbana-Champaign, 1002 W. Green Street, Urbana, IL 61801, USA
[10] Department of Physics and Astronomy, Rutgers, The State University of New Jersey, Piscataway, NJ 08854, USA
[11] Observatories of the Carnegie Institution for Science, 813 Santa Barbara St., Pasadena, CA 91101, USA
[12] INAF-Osservatorio Astronomico di Padova, vicolo dell Osservatorio 5, 35122 Padova, Italy
[13] George P. and Cynthia Woods Mitchell Institute for Fundamental Physics & Astronomy, Texas A. & M. University, Department of Physics, 4242 Tamu, College Station, TX 77843, USA
[14] Center for Mathematical Modelling, Universidad de Chile, Avenida Blanco Encalada 2120 Piso 7, Santiago, Chile
[15] University of Texas at Austin, 1 University Station C1400, Austin, TX 78712-0259, USA
[16] Departamento Ciencias Fosicas, Universidad Andres Bello, Av. Republica 252, Santiago, Chile

ABSTRACT

We present ultraviolet through near-infrared (NIR) broadband photometry, and visual-wavelength and NIR spectroscopy of the Type Iax supernova (SN) 2012Z. The data set consists of both early- and late-time observations, including the first late phase NIR spectrum obtained for a spectroscopically classified SN Iax. Simple model calculations of its bolometric light curve suggest SN 2012Z produced $\sim 0.3~M_\odot$ of ^{56}Ni, ejected about a Chandrasekhar mass of material, and had an explosion energy of $\sim 10^{51}$ erg, making it one of the brightest ($M_B = -18.3$ mag) and most energetic SN Iax yet observed. The late phase (+269d) NIR spectrum of SN 2012Z is found to broadly resemble similar epoch spectra of normal SNe Ia; however, like other SNe Iax, corresponding visual-wavelength spectra differ substantially from all supernova types. Constraints from the distribution of intermediate mass elements, e.g., silicon and magnesium, indicate that the outer ejecta did not experience significant mixing during or after burning, and the late phase NIR line profiles suggests most of the ^{56}Ni is produced during high density burning. The various observational properties of SN 2012Z are found to be consistent with the theoretical expectations of a Chandrasekhar mass white dwarf progenitor that experiences a pulsational delayed detonation, which produced several tenths of a solar mass of ^{56}Ni during the deflagration burning phase and little (or no) ^{56}Ni during the detonation phase. Within this scenario only a moderate amount of Rayleigh-Taylor mixing occurs both during the deflagration and fallback phase of the pulsation, and the layered structure of the intermediate mass elements is a product of the subsequent denotation phase. The fact that the SNe Iax population does not follow a tight brightness-decline relation similar to SNe Ia can then be understood in the framework of variable amounts of mixing during pulsational rebound and variable amounts of ^{56}Ni production during the early subsonic phase of expansion.

Key words. supernovae: individual: SN 2012Z – supernovae: individual: SN 2005hk – supernovae: general

1. Introduction

Over recent years dedicated non-targeted and targeted transient search programs have revealed the existence of a multitude of peculiar transients lurking in the nearby Universe. A particular group of objects that share a number of commonalities, warranting their own spectroscopic designation are Type Iax supernovae (see Foley et al. 2013, for a review). Supernova (SN) 2002cx serves as the prototypical example of what was originally entitled by Li et al. (2003) as "The Most Peculiar Known Type Ia Supernova". Since the discovery of SN 2002cx, it has become clear that they are not all that rare. They have been estimated to account for 5–30% of the overall SNe Ia rate (Li et al. 2011; Foley et al. 2013; White et al. 2014). SNe Iax are characterized by a number of observational peculiarities, including, among others, a significant range in peak luminosity ($M_B \sim -14$ to -18 mag); spectral signatures characteristic of over luminous 1991T-like SNe Ia such as blue continua at early phases and iron lines observed at all epochs; expansion velocities that are about half (4000 to 9000 km s^{-1}) of what is observed in normal SNe Ia (10 000 to 15 000 km s^{-1}) at similar epochs; and late phase optical spectra which bear little to no resemblance to other types of supernovae.

Detailed studies of the light curves and spectra of well-observed SNe Iax indicate that they generate between ~0.003–0.30 $M_\odot$ of ^{56}Ni, and have explosion energies ranging from ~10^{49}–10^{51} erg. The progenitors of the entire class of SNe Iax are unknown and are a matter of open debate. Recent efforts to model bright SNe Iax (e.g., SN 2005hk) suggest that their origins may lie with the partial thermonuclear incineration of a carbon-oxygen Chandrasekhar mass white dwarf (WD), which leaves a bound remnant (Jordan et al. 2012; Kromer et al. 2013; Fink et al. 2013). However, pure deflagration models are currently unable to account for the stratified distribution of intermediate mass elements (IMEs) that are inferred from the spectroscopic observations of some bright SNe Iax. All current deflagration models produce significant mixing throughout the explosion (Livne & Arnett 1993; Livne 1993; Khokhlov 1995; Gamezo et al. 2003; Reinecke et al. 2002; Gamezo et al. 2005; Röpke et al. 2007; Seitenzahl et al. 2009, 2013), and it is unclear whether additional physics can sufficiently suppress mixing in deflagrations (Hoeflich et al. 2013). This leaves open room for other possible progenitor scenarios, such as for example, the partial thermonuclear disruption of helium accreting sub-Chandrasekhar mass white dwarfs (Wang et al. 2013) or mergers (Piersanti et al. 2003). In this paper we discuss an alternative scenario that explains most of the features of the recently observed Type Iax SN 2012Z (Foley et al. 2013), as well as some other members of the SNe Iax class. However, it is important to keep in mind that SNe Iax are not a homogeneous class and several explosion scenarios may contribute to the entire observed population.

Recently we studied SNe 2008ha and 2010ae, which are the least luminous Type Iax objects yet observed (Stritzinger et al. 2014). Here, our attention is turned towards the bright end of the luminosity distribution of SNe Iax. Specifically we present ultraviolet (UV), optical and near-infrared (NIR) observations of SN 2012Z. The data reveal that this object bears a striking resemblance to the well-observed Type Iax SN 2005hk (Chornock et al. 2006; Phillips et al. 2007; Sahu et al. 2008; Maund et al. 2010; McCully et al. 2014a), and further indicates that SN 2012Z is among the brightest and most energetic SN Iax yet observed. The majority of the data presented in this study were obtained as part of the Carnegie Supernova Project-II (CSP-II), which

is a four year NSF-funded SN followup program aimed at obtaining optical and NIR observations of ~100 SNe Ia located in the Hubble flow. The CSP-II is placing a particular emphasis on carrying out detailed NIR spectroscopy, and as a result, this paper presents the most comprehensive NIR time series of a SN Iax. We also note that revised optical and NIR photometry of SN 2005hk are presented in the Appendix. Since these data were first published by Phillips et al. (2007), the images of SN 2005hk have undergone proper host-galaxy template subtraction, and as well, the calibration of the local sequence has been improved.

In a companion paper, we report on the detection of a luminous and blue point source coincident with the location of SN 2012Z in pre-explosion *Hubble* Space Telescope (HST) images (McCully et al. 2014b). This direct detection is consistent with a helium-star donating material to an accreting white dwarf as the progenitor for SN 2012Z. Followup HST observations have the potential to determine if the progenitor system was correctly identified and consistent with such a model.

The observations of SN 2012Z presented here provide unique coverage of the light curve and time evolution of the spectra at both optical and NIR wavelengths for a SN Iax. In supernovae, we are able to peer into deeper layers of the ejecta over time, and therefore, our observations allow us to probe the entire envelope structure. The nature of SNe Iax is under discussion, as are many aspects of the explosion physics and the nature of the variations observed within SNe Ia. A comprehensive discussion of the latter point is beyond the scope of this paper and therefore, we refer the reader to Hoeflich (2006), Hoeflich et al. (2013), and references therein. In what will follow, we discuss the various constraints on the underlying progenitor provided by individual observational components, as well as compare SN 2012Z to other SNe Ia and SNe Iax. As a reference scenario to compare SN 2012Z with normal SNe Ia, we adopt one of a series of delayed-detonation models of the later because it is readily available, fits many observational properties of SNe Ia, and can be regarded as a limiting case for one of the models discussed below. The goal of this work is not to rule out a specific model, but rather to piece together the arguments within all scenarios discussed in the literature. By considering the individual observational constraints of SN 2012Z and confronting them with various scenarios, we suggest a unified picture that may explain the nature of at least some SNe Iax.

1.1. Supernova 2012Z

SN 2012Z was discovered with the KAIT telescope as a part of LOSS (see Filippenko et al. 2001; Filippenko 2005) on 2012 Jan. 29.15 UT, at an apparent unfiltered magnitude of 17.6 (Cenko et al. 2012). With J2000.0 coordinates of $\alpha = 03^\mathrm{h}22^\mathrm{m}05\overset{s}{.}35$ and $\delta = -15°23'15''\!.6$, the position of this supernova is 14$''$.6 West and 42$''$.1 North from the center of the SA(s)bc galaxy NGC 1309. Figure 1 contains an image of the host galaxy with SN 2012Z indicated. Spectroscopic confirmation obtained three days after the discovery indicated that this was a SN Iax on the rise (Cenko et al. 2012).

NED lists the redshift of NGC 1309 as $cz = 2,136$ km s^{-1} or $z = 0.007125$. NGC 1309 has a number of Cepheid-based distance measurements, and as well has hosted the normal Type Ia SN 2002fk (Riess et al. 2009; Cartier et al. 2014). A recent recalibration of the distance scale by Riess et al. (2011), provides an up-to-date Cepheid based distance to NGC 1309 of 33.0 ± 1.4 Mpc or $\mu = 32.59 \pm 0.09$. Given the accuracy of this distance measurement, it is adopted in this paper to set the absolute flux scale of SN 2012Z.

Fig. 1. Composite image of the SA(s)bc galaxy NGC 1309, with the position of SN 2012Z indicated. North is up and East is left.

2. Observations

2.1. Ultraviolet, optical, and NIR imaging

SN 2012Z was observed from space with the UVOT camera aboard the *Swift* X-ray telescope (Burrows et al. 2005; Roming et al. 2005). Up to 13 epochs of UV *uvw2*, *uvm2*, and *uvw1*-band imaging was obtained over the duration of a month. Template images of the host obtained during early 2013 were used to estimate the background emission at the position of the SN. Aperture photometry of the SN was then computed as described by Brown et al. (2009), using the calibration zero-points and sensitivity corrections from Breeveld et al. (2011). The final UV photometry is listed in Table 1.

Optical (*ugriBV*) imaging of SN 2012Z was initiated near the end of the first campaign of the CSP-II with the *Swope* 1.0 m (+SITe3 direct CCD camera) telescope at the Las Campanas Observatory (LCO). In addition, NIR (*YJH*) imaging was also obtained with the *du Pont* 2.5 m telescope (+RetroCam). All CSP-II imaging was processed in the standard manner, following the procedures described by Hamuy et al. (2006) and Contreras et al. (2010).

Before computing photometry of the SN, galaxy subtraction was performed on all science images. High signal-to-noise optical and NIR template images of NGC 1309 were obtained under favorable seeing conditions with the *du Pont* telescope between the 10th and the 17th of October 2013. Multiple exposures were stacked to create master templates, which were then subtracted from the science images following the techniques described by Contreras et al. (2010).

PSF photometry of SN 2012Z was computed differentially with respect to a local sequence of stars in the field of NGC 1309. The optical sequence consists of 17 stars calibrated with respect to Landolt (1992; *BV*) and Smith et al. (2002; *ugri*) photometric standard fields, which were observed over the course of multiple photometric nights. The NIR local sequence, on the other hand, contains 6 stars calibrated relative to Persson et al. (1998) standards also observed over multiple photometric nights. As the Persson et al. (1998) catalog of standards does not include *Y*-band photometry, the *Y*-band local sequence was calibrated relative to unpublished *Y*-band photometry of a subset of the Persson et al. standards. The standard star *Y*-band photometry was computed from multiple observations conducted at LCO as part of the CSP-I (Hamuy et al. 2006). Final absolute photometry of the optical and NIR local sequence in the *natural* system is listed in Table 2. The quoted uncertainty for each magnitude corresponds to the weighted average of the instrumental errors of the photometry during the nights photometric standard fields were observed.

With photometry of the local sequences and template subtracted science images in hand, PSF photometry of SN 2012Z was computed as prescribed by Contreras et al. (2010). The definitive optical and NIR photometry in the *natural* photometric system of the *Swope* and *du Pont* telescopes is listed in Tables 3 and 4, respectively. The uncertainties accompanying each photometric measurement correspond to the sum in quadrature of the instrumental error and the nightly zero-point error. The early phase UV, optical, and NIR light curves of SN 2012Z are plotted relative to the time of *B*-band maximum (hereafter $T(B)_{max}$) in Fig. 2. We note that a single epoch of *BVi*-band optical photometry was also obtained at late phases. This epoch of data is used below to provide a lower limit on the UVOIR (UltraViolet Optical near-IR) flux at +266d (see below).

2.2. Optical and NIR spectroscopy

Five epochs of early phase (+2d to +21d), low-resolution visual-wavelength spectroscopy of SN 2012Z was obtained by the CSP-II with the Nordic Optical Telescope (NOT+Alfosc), and the *Magellan Clay* telescope (+LDSS3). In addition, a single high-resolution optical spectrum was obtained on −7d with the
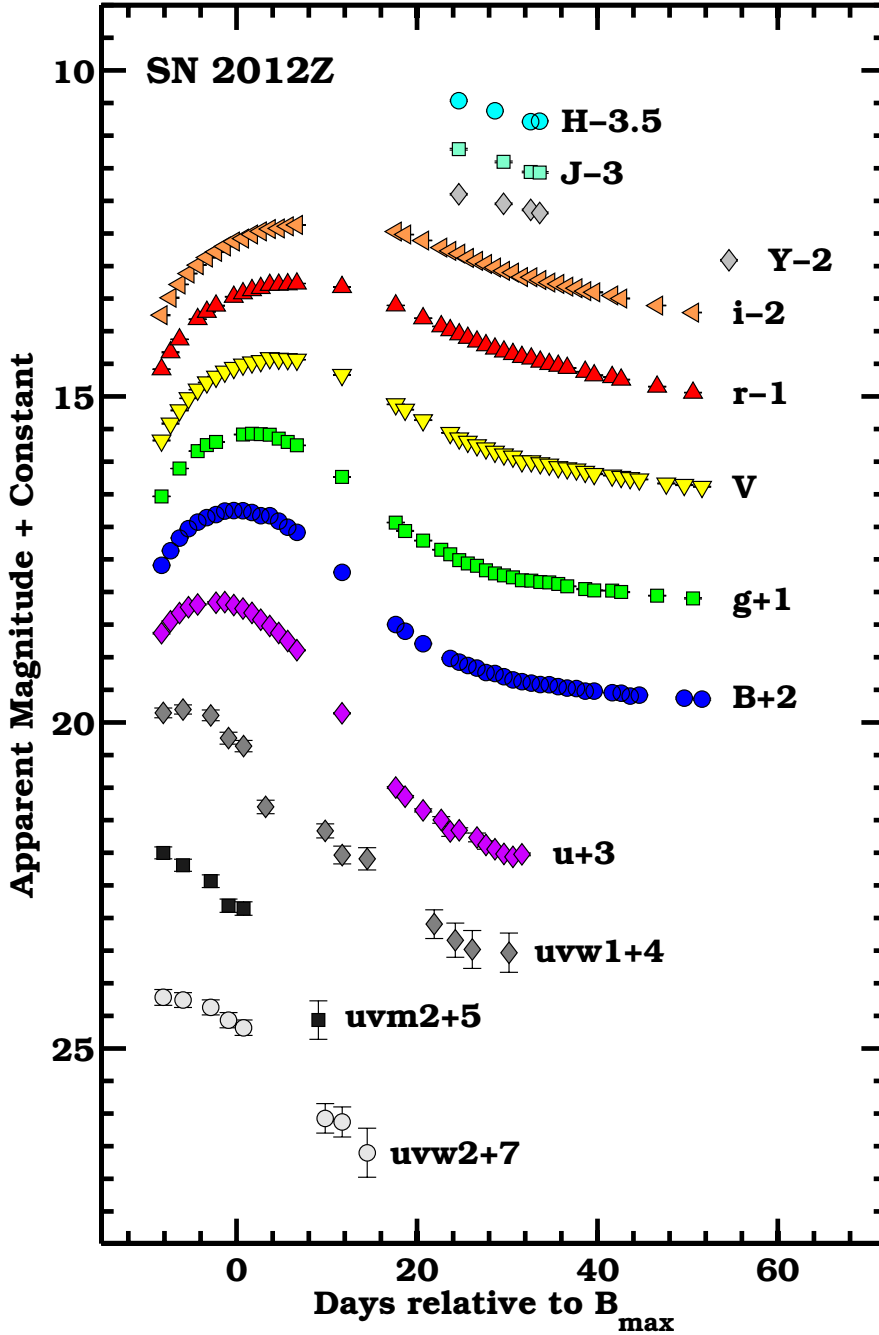
Fig. 2. UV, optical, and NIR light curves of SN 2012Z.

Magellan Inamori Kyocera Echelle (MIKE; Bernstein et al. 2003) spectrograph attached to the *Magellan Clay* telescope. All low-resolution spectra were reduced in the standard manner using IRAF[1] scripts, while the high-resolution spectrum was reduced using the MIKE pipeline (Kelson 2003) following the methods described by Simon et al. (2010). Complementing the early spectroscopy are 3 epochs of late phase (+194d to +248d), low-resolution spectra, which were obtained with SALT (+ RSS), the *du Pont* (+WFCCD) and Keck (+DEIMOS) telescopes.

A summary of our spectroscopic observations and those of Foley et al. (2013) is provided in the spectroscopic journal given in Table 5. As seen in Fig. 3, our early phase spectra nicely complement the previously published spectra of SN 2012Z. The 3 late phase visual-wavelength spectra are plotted in Fig. 4.

Ten epochs of NIR spectroscopy were also obtained for SN 2012Z, and details concerning these observations are provided in Table 5. This includes 5 epochs taken with the *Magellan Baade* telescope (+FIRE), 4 epochs with the Very Large Telescope (VLT+ISAAC), and finally, one epoch with the New Technology Telescope (NTT+Sofi). The FIRE spectra were reduced as described by Hsiao et al. (2013), while the VLT and NTT spectra were reduced as described by Smartt et al. (2013). The NIR spectroscopic sequence plotted in Fig. 5 extends from −7d to +269d, and consists of the most comprehensive NIR time-series yet obtained for a SN Iax, including the first late phase NIR spectrum.
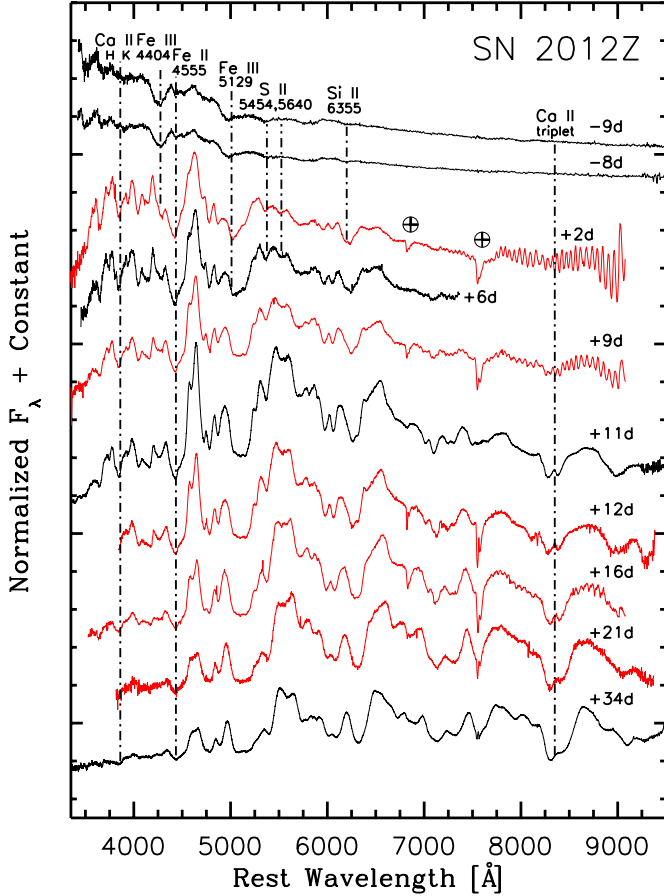
---

[1] The image Reduction and Analysis Facility (IRAF) is maintained and distributed by the Association of Universities for Research in Astronomy, under the cooperative agreement with the National Science Foundation.

Fig. 3. Early phase, visual-wavelength spectroscopy of SN 2012Z plotted in the rest frame of the host galaxy. A subset of spectra from Foley et al. (2013) are plotted in black, and our previously unpublished spectra are shown in red. Phase relative to $T(B)_{max}$ is listed to the right of each spectrum. Telluric features are indicated with an Earth symbol. The spectra obtained on +2d, +9d, and +16d suffer from moderate fringing.
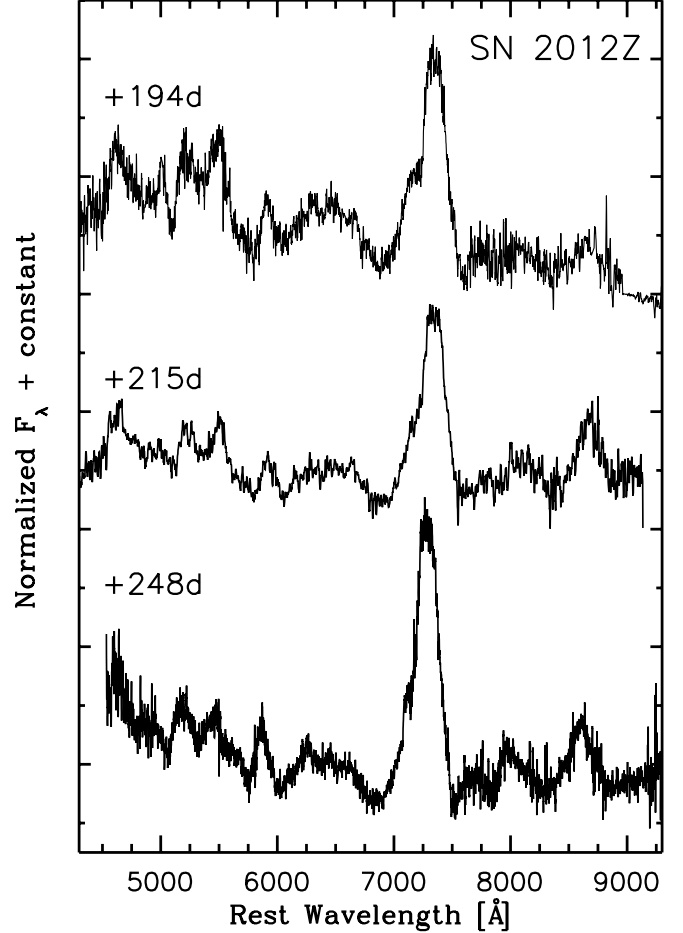

Fig. 4. Late phase, visual-wavelength spectra of SN 2012Z obtained on +194d, +215d and +248d. Each spectrum has been slightly smoothed for presentation purposes.

3. Dust extinction

The Milky Way color excess in the direction of NGC 1309 is listed in NED to be $E(B-V)_{MW} = 0.035 \pm 0.012$ mag (Schlafly & Finkbeiner 2011), which when adopting a Fitzpatrick (1999) reddening law characterized by an $R_V = 3.1$, corresponds to $A_V = 0.11$ mag.

Estimating the level of reddening that affects the emission of supernovae due to dust external to the Milky Way (MW) is a challenging prospect, particularly for peculiar types that do not have well-defined intrinsic colors. One must therefore find alternative methods to estimate host reddening. In the case of SN 2012Z, we first examine the host-galaxy color-excess value inferred from the broadband optical and NIR light curves of the normal Type Ia SN 2002fk, which occurred in an inner region of NGC 1309. From a detailed analysis of its broadband colors, Cartier et al. (2014) estimate the color excess along the line of sight of SN 2002fk to be $E(B-V)_{host} = 0.057 \pm 0.036$ mag. As SN 2012Z is located in the outskirts of NGC 1309 one may expect that it suffered a similar level or even less reddening.

Using the high-resolution MIKE spectrum, we next explored if a more direct handle on the host reddening could be obtained via column density measurements of neutral sodium and potassium inferred from host absorption components of the Na I D $\lambda\lambda5890$, 5896 and K I $\lambda\lambda7665$, 7699 doublets. Line fits

computed using the Voigt profile fitting program VPFIT provided column densities of $\log_{10} N_{Na I} = 12.79 \pm 0.09$ cm^{-2} and $\log_{10} N_{K I} = 11.30 \pm 0.09$ cm^{-2}. These values give a $N_{Na I}$ to $N_{K I}$ ratio that is perfectly normal for the MW (see Phillips et al. 2013, Fig. 13). Adopting the MW relations between $\log_{10} N_{Na I}$ and $\log_{10} N_{K I}$ vs. A_V, as derived by Phillips et al. (2013, see their Eqs. (4) and (5)), implies visual extinction values of $A_V(\text{Na I}) = 0.45 \pm 0.24$ mag and $A_V(\text{K I}) = 0.50 \pm 0.36$ mag, respectively.

Phillips et al. (2013) also recently showed that the 5780 Å diffuse interstellar band (DIB) can provide a robust means to estimate host reddening. Under close inspection of the high-resolution spectrum of SN 2012Z this feature is not detectable. However from the signal-to-noise ratio of the MIKE spectrum at the expected position of this feature, a 3σ upper limit on the equivalent width of $EW(5780) \leq 35$ mÅ is estimated. Adopting the Phillips et al. (2013, see their Eq. (6)) MW relation that connects $\log_{10} EW(5780)$ to A_V then implies an $A_V \leq 0.18 \pm 0.09$ mag. This value and those derived from Na I and K I doublets are generally consistent, and when combined via a weighted average imply an $A_V = 0.23 \pm 0.08$ mag, which when adopting an $R_V = 3.1$, corresponds to a host galaxy color excess $E(B-V)_{host} = 0.07 \pm 0.03$ mag. Interestingly, this value is fully consistent with what is derived from the broadband colors of SN 2002fk. In what follows we adopt this value for the host reddening of SN 2012Z, and when combining with the MW component, gives the total color excess $E(B-V)_{tot} = 0.11 \pm 0.03$ mag.

Table 6. Optical light curve parameters of SNe 2005hk and 2012Z.

Filter	Peak time (JD$-2\,450\,000$)	Peak Obs. (mag)	Δm_{15} (mag)	Peak Abs. (mag)
	SN 2005hk			
u	3682.54 ± 0.36	16.27 ± 0.01	1.96 ± 0.07	-17.73 ± 0.25
g	3685.92 ± 0.08	15.78 ± 0.01	1.36 ± 0.01	-18.08 ± 0.25
r	3691.66 ± 0.23	15.68 ± 0.01	0.70 ± 0.02	-18.07 ± 0.25
i	3695.27 ± 0.16	15.80 ± 0.01	0.60 ± 0.01	-17.88 ± 0.25
B	3685.16 ± 0.07	15.91 ± 0.01	1.62 ± 0.01	-18.00 ± 0.25
V	3688.28 ± 0.14	15.73 ± 0.01	0.92 ± 0.01	-18.07 ± 0.25
	SN 2012Z			
u	5965.48 ± 0.35	15.16 ± 0.01	1.92 ± 0.08	-17.95 ± 0.09
g	5969.78 ± 0.12	14.57 ± 0.01	1.30 ± 0.01	-18.40 ± 0.09
r	5975.26 ± 0.33	14.27 ± 0.01	0.66 ± 0.02	-18.60 ± 0.09
i	5978.46 ± 0.53	14.34 ± 0.01	0.54 ± 0.04	-18.46 ± 0.09
B	5967.89 ± 0.11	14.75 ± 0.01	1.43 ± 0.02	-18.27 ± 0.09
V	5972.74 ± 0.14	14.42 ± 0.01	0.89 ± 0.01	-18.50 ± 0.09
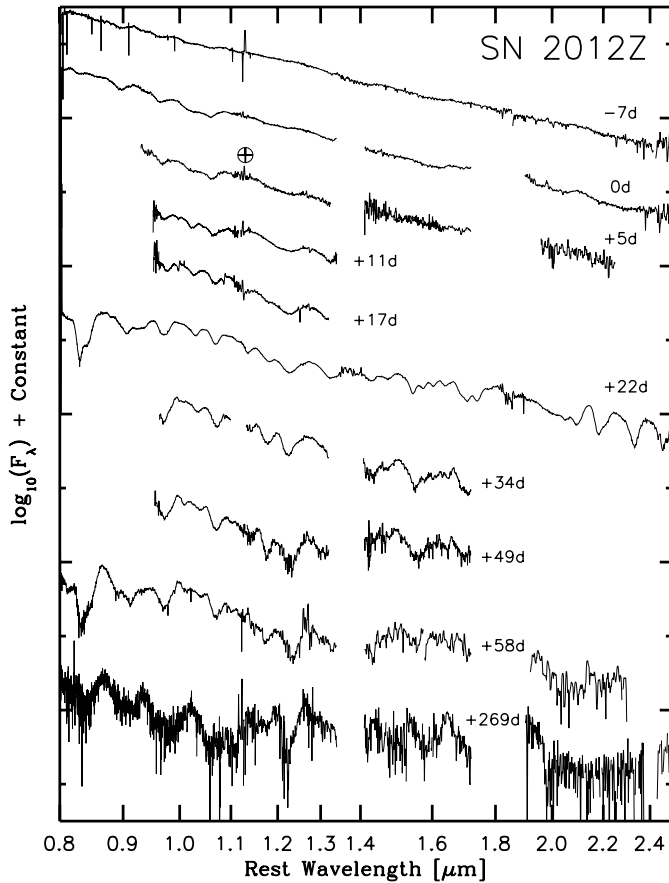
Fig. 5. NIR-wavelength spectroscopy of SN 2012Z. Phase relative to $T(B)_{\mathrm{max}}$ is listed to the right of each spectrum.

4. Results

4.1. UV, optical and NIR light curves

The photospheric phase optical light curves of SN 2012Z plotted in Fig. 2 consist of dense photometric coverage, while the UV light curves are of considerably lower quality, and the NIR light curves contain only a handful of epochs, beginning well after maximum. The optical light curves reveal the characteristic bell-shape appearance that is typical of stripped-envelope supernovae, indicative of a rather low ejecta mass. Similar to

other bright SNe Iax, the r- and i-band light curves appear broad and slowly evolving as compared to the bluer bands. In addition, the r- and i-band light curves show no evidence of a secondary maximum, which is a defining characteristic of normal SNe Ia (Hamuy et al. 1996). Interestingly, the *uvw2*- and *uvm2*-band light curve are found to be already declining 8 days before $T(B_{\mathrm{max}})$, while the *uvw1* light curve appear to be at peak brightness. Clearly, the UV light curves reach maximum well before the optical light curves.

Light curve parameters were measured from Gaussian Process functional fits to the optical light curves using software contained within the light-curve fitter SNooPy (Burns et al. 2011). The fit parameters consist of: (i.) the time of maximum; (ii.) peak apparent magnitude and; (iii.) an estimate of the decline-rate parameter, Δm_{15}[2]. These fit parameters are listed in Table 6, along with those measured from the revised photometry of SN 2005hk (see Appendix), accompanied with robust uncertainties derived via Monte Carlo simulations. The light-curve fit parameters indicate that the bluer the light curve the earlier maximum is reached, with a $\Delta t \approx 13$ day difference between the time of u- and i-band maxima, and the redder the light curve the smaller its decline-rate. The decline-rate ranges from as much as 1.92 ± 0.08 mag in the u band, all the way down to 0.54 ± 0.04 mag in the i band.

Figure 7 shows the $(B - V)$, $(V - r)$ and $(V - i)$ color evolution of SN 2012Z compared to that of the Type Iax SN 2005hk and the normal, un-reddened Type Ia SN 2006ax. The color curves of both SNe Iax have been corrected for MW and host reddening. Overall the colors and the color evolution of SNe 2005hk and 2012Z are very similar, with the former appearing marginally bluer. At the start of the observations the color curves of SN 2012Z are at their bluest. They then slowly evolve and reach a maximum value in the red around 20 days past $T(B)_{\mathrm{max}}$, at which point an inflection is observed followed by a linear evolution with a negative slope. The color evolution of the two SNe Iax also have a similar overall shape to normal SNe Ia, but with colors that are consistently redder as the supernovae evolve. It will be interesting to see in the future, as more well-observed, bright SNe Iax become available, if this family of

---

[2] The light curve decline-rate parameter, Δm_{15}, is defined as the magnitude change from the time of maximum brightness to 15 days later. For normal SNe Ia, Δm_{15} correlates with the peak absolute luminosity in such a way that more luminous objects exhibit smaller Δm_{15} values (Phillips 1993), however this is not the case for SNe Iax (see, e.g., Fig. 6).
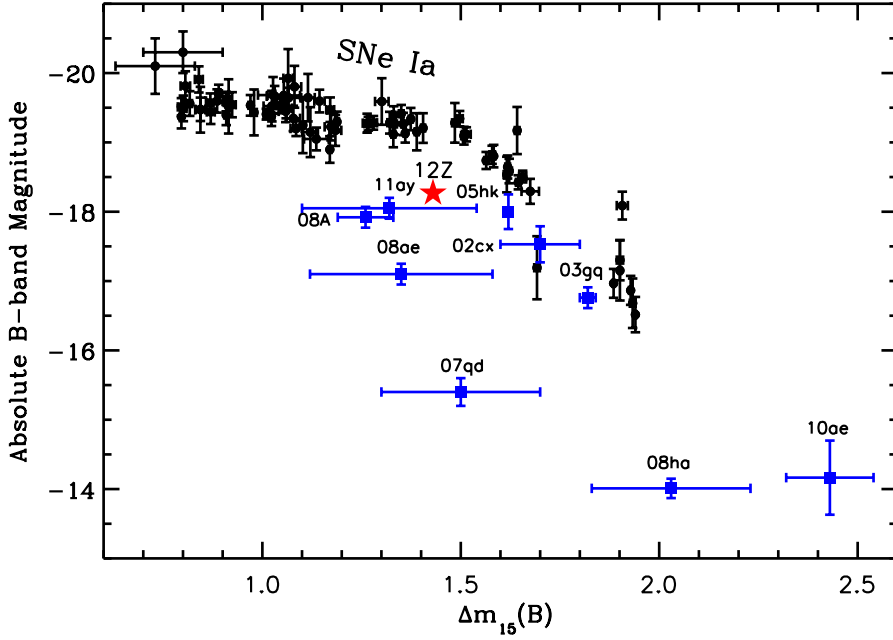
Fig. 6. M_B vs. $\Delta m_{15}(B)$ for a sample of CSP SNe Ia (black dots), a handful of SNe Iax (blue squares) that span their full range in luminosity, and SN 2012Z (red star). We note the error bars associated with SN 2012Z are smaller than its symbol size. The comparison SNe Iax plotted are SN 2002cx (Li et al. 2003; Phillips et al. 2007), SN 2003gq (see Foley et al. 2013, and references therein), SN 2005hk (Phillips et al. 2007), SN 2007qd (McClelland et al. 2010), SN 2008A (see Foley et al. 2013, and references therein), SN 2008ge (Foley et al. 2013), SN 2008ha (Stritzinger et al. 2014), SN 2010ae (Stritzinger et al. 2014), and SN 2011ay (Brown, priv. comm.).
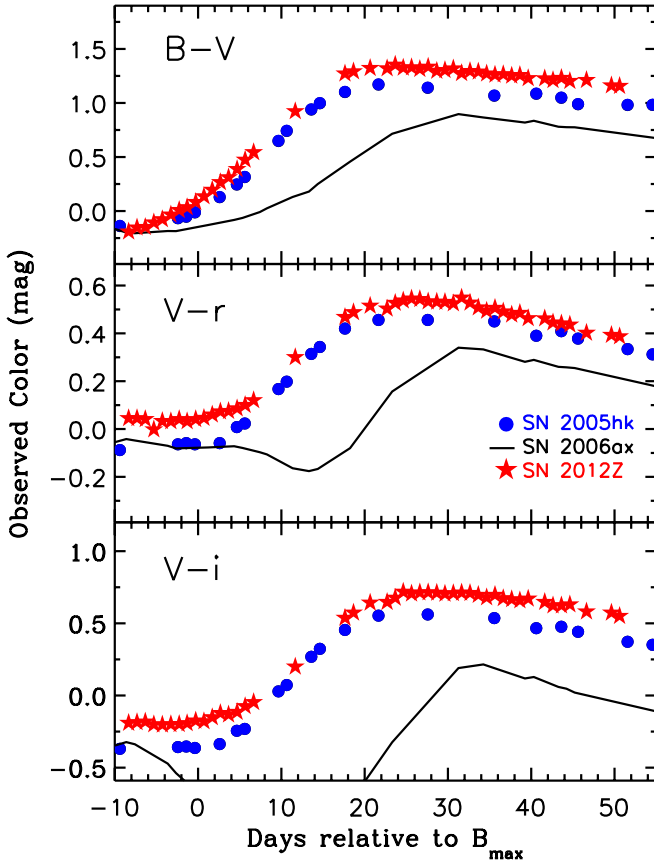
4.2. Absolute magnitudes, UVOIR light curve, and light curve modeling

With estimates of peak apparent magnitude for the *ugriBV* bands in hand, peak absolute magnitudes were computed adopting an $E(B-V)_{tot} = 0.11 \pm 0.03$ mag and the direct distance measurement $\mu = 32.59 \pm 0.09$ mag. The resulting peak values are listed in Table 6[3], with accompanying uncertainties that account for both the error in the fit to the time of maximum, and the error associated with the distance to the host galaxy. Reaching an absolute peak *B*-band magnitude (M_B) $\approx -18.3 \pm 0.1$ with $\Delta m_{15}(B) = 1.43 \pm 0.02$ mag, SN 2012Z is among the brightest and slowest declining SN Iax yet observed. This is demonstrated in Fig. 6, where the location of SN 2012Z in the M_B vs. Δm_{15} diagram is shown compared to a handful of other well-observed SNe Iax, and an extended sample of SNe Ia observed by the CSP.

Armed with the broadband photometry of SNe 2005hk and 2012Z, we proceeded to construct UVOIR bolometric light curves. For SN 2005hk we adopted the early phase photometry presented in Appendix A, as well as the late phase photometry published by Sahu et al. (2008). The early phase filtered light curves of both objects were fit with spline functions, which allowed us to fill in missing gaps in the data based on interpolation. For SN 2012Z the *u*-band light curve was extended so that its temporal coverage matched that of the other optical filters. To do so, we resorted to extrapolation by adopting an average $(u-B)$ color derived from the last three epochs in which *u*-band photometry was obtained.

With the definitive observed light curves in hand, the photometry was corrected for extinction, and then converted to flux at the effective wavelength of each passband. This allowed us to construct SEDs spanning from ∼300 to 2500 nm. The full series of SEDs were then summed over wavelength using a trapezoidal integration technique, assuming zero flux beyond the limits of integration. Owing to our limited NIR photometric coverage of SN 2012Z it was necessary to account for the NIR contribution of the flux. Given the close resemblance between the peak

Fig. 7. $(B-V)$, $(V-r)$, and $(V-i)$ color evolution of SN 2012Z (red stars), compared to the Type Iax SN 2005hk (blue dots) and the un-reddened, normal Type Ia SN 2006ax (solid line). The photometry of SN 2006ax is taken from Contreras et al. (2010). The color curves of SNe 2005hk and 2012Z have been corrected for Milky Way and host extinction adopting $E(B-V)_{tot} = 0.112$ mag (Chornock et al. 2006; Phillips et al. 2007) and $E(B-V)_{tot} = 0.105$ mag, respectively, while the color curves of SN 2006ax have been corrected for Milky Way reddening.

objects displays intrinsic colors or color evolution which could allow an accurate estimation of the host extinction.

---

[3] To derive absolute magnitudes of SN 2005hk (and absolute luminosity, see Sect. 4.2), we have adopted a distance modulus of $\mu = 33.46 \pm 0.27$ mag (Phillips et al. 2007) and the total color excess value $E(B-V)_{host} = 0.11$ mag.
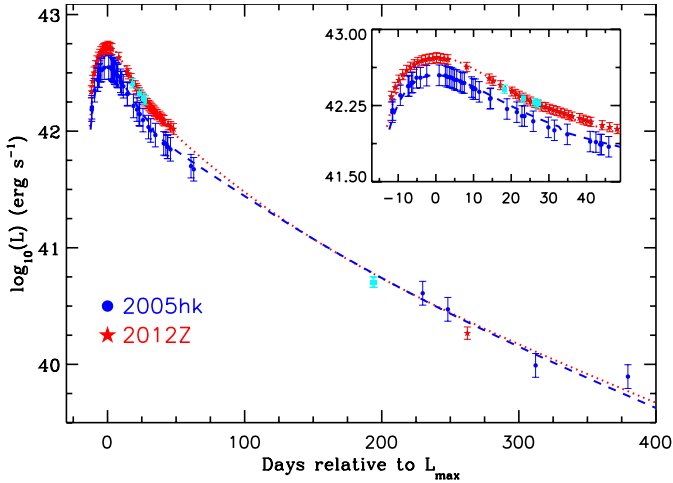
Fig. 8. UVOIR light curves of SNe 2005hk and 2012Z, over-plotted by model fits based on Arnett's equations. The model fits provide estimates of the M_{Ni}, M_{ej} and E_K (see Sect. 4.2). Also plotted as filled cyan squares are UVOIR flux points of SN 2012Z computed using its optical and NIR photometry. These points are in excellent agreement with the UVOIR flux points of SN 2012Z, as computed using the NIR flux contribution estimated from SN 2005hk. We note that the error bars are appreciably larger for SN 2005hk, due to its larger uncertainty in distance.

luminosity, light curve shape (see Sect. 6), and color evolution between SNe 2005hk and SN 2012Z, we resorted to adopting the fraction of NIR flux estimated from the full optical/NIR spectral energy distribution (SED) of SN 2005hk. The final UVOIR light curves of SNe 2005hk and SN 2012Z are plotted in Fig. 8, with the associated error-bars accounting for uncertainties in the photometry, total reddening, and distance. We note that also over plotted in Fig. 8 are a handful of flux points of SN 2012Z, which were computed using its optical *and* limited NIR photometry. These points are in full agreement with the UVOIR flux points of SN 2012Z that contain the contribution of NIR flux estimated from SN 2005hk.

To derive rough estimates of the explosion parameters for these SNe Iax, we turned to toy model fits of the UVOIR light curves based on Arnett's equations (Arnett 1982), following the implementation described by Valenti et al. (2008). The most interesting parameters are the amount of radioactive ^{56}Ni synthesized during the explosion, the ejecta mass (M_{ej}), and the explosion energy (E_k). The model calculations rely upon a number of underlying assumptions and therefore the results should be approached with caution. With this caveat in mind, the model assumptions include: complete energy deposition supplied from the radioactive decay chain ^{56}Ni→^{56}Co→^{56}Fe, spherical symmetry, homologous expansion of the ejecta, no appreciable mixing of ^{56}Ni, a constant optical opacity (i.e., $\kappa_{opt} = 0.1$ cm^2 g^{-1}), and the diffusion approximation for photons. A crucial input parameter in computing the model calculations is a measure of the expansion velocity (v_{ph}) of the ejecta. From a detailed inspection of the optical spectral features of SN 2012Z (see Sect. 4.3), this parameter is estimated to range between $7000 \lesssim v_{ph} \lesssim 9000$ km s^{-1}. In the case of SN 2005hk, based on velocity measurements presented by Phillips et al. (2007) and McCully et al. (2014a), we infer the range $5000 \lesssim v_{ph} \lesssim 7000$ km s^{-1}. For both objects a grid of models was computed that encompasses the appropriate range of v_{ph}. Final best-fit model calculations are over-plotted in Fig. 8. The range of explosion parameters computed for SN 2005hk are $M_{Ni} = 0.15-0.20$ $M_{\odot}$, $M_{ej} = 1.5-2.0$ $M_{\odot}$ and $E_k = 0.4-1.2 \times 10^{51}$ erg; while those

of SN 2012Z are $M_{Ni} = 0.25-0.29$ $M_{\odot}$, $M_{ej} = 1.4-2.6$ $M_{\odot}$ and $E_k = 0.7-2.8 \times 10^{51}$ erg.

These rough estimates of the explosion parameters are in essence based on Arnett's Rule and the the photospheric expansion velocity, v_{phot}. It should be stressed that a portion of the large range in the estimated parameters is due to the degeneracy between the E_k, M_{Ni} and M_{ej}, and the reliance on, in effect, a single bolometric light curve. Furthermore, we note that the estimated values of the various explosion parameters do not capture enough of the physical variations displayed by the various suite of SNe Ia explosion models found in the literature. Even for normal SNe Ia, Arnett's Rule is but a useful means of obtaining a qualitative understanding of the relation between the mass of ^{56}Ni produced and the peak brightness. In particular, due to the strong temperature dependence of the opacity, opacities vary by two and a half orders of magnitude at each phase of the evolution of the supernova (Hoeflich et al. 1992). This opacity variation is required in order to reproduce the brightness decline-rate relation (Hoeflich et al. 1996; Nugent et al. 1995b; Pinto & Eastman 2001; Maeda et al. 2003; Baron et al. 2012). Attempts to account for both γ rays escape and energy stored within the expanding ejecta due to variations in the diffusion time and non-constant opacities, have led to further parameterization to the standard form of Arnett's Rule. This is normally accomplished by the introduction of the parameter, α, which leads to $L_{bol}^{max} \approx \alpha \dot{S}(t_{max})$. The parameter α is thought to lie somewhere in the range $0.7 \lesssim \alpha \lesssim 1.5$ (e.g., Branch 1992; Khokhlov et al. 1993; Hoeflich & Khokhlov 1996)[4]. With such a large range in α, attempts to use Arnett's Rule for quantitative analysis will only be accurate to about 50%.

SNe Iax light curves are characterized by a short rise time as compared with normal SNe Ia. The hydrodynamics is determined by the total ejected mass and the total energy produced by thermonuclear fusion; however, the light curves are determined not by the total mass, but rather by the optical depths, that is the product of the column density and the opacities. As the opacities vary by several orders of magnitude over time as well as varying with abundances and ionization stage, a change in the opacity by a factor of two is equivalent to a variation in the mass by $\sim\sqrt{2}$. Choosing a constant opacity to fit with the rise-time is equivalent to fixing the mass scale. In Arnett (1982) the opacity is chosen to give the rise time for a Chandrasekhar mass explosion.

In Sect. 5 we attempt to gain an additional handle on the explosion parameters of SN 2012Z through comparison of the observations to modern explosion models.

4.3. Early phase spectroscopy

The sequence of early phase visual-wavelength spectra plotted in Fig. 3 reveals all of the quintessential features of a SN Iax located at the bright end of the luminosity distribution. At the earliest epochs, SN 2012Z exhibits a hot continuum dotted with prevalent iron features. These characteristics are reminiscent of early spectra of luminous 1991T-like SNe Ia, however, they differ substantially at late phases. The blue portion of the −9d spectrum exhibits clear features produced by Ca II H&K, Fe II λ4555 and Fe III $\lambda\lambda$4404, 5129, while red-wards of ∼5000 Å the spectrum is relatively smooth, only showing subtle notches at the expected locations of the IMEs S II $\lambda\lambda$5454, 5640 and Si II λ6355. By maximum, the strengths of these IME features mildly increase, however soon thereafter, their presence is diluted by the emergence of numerous permitted lines of Fe II and Co II

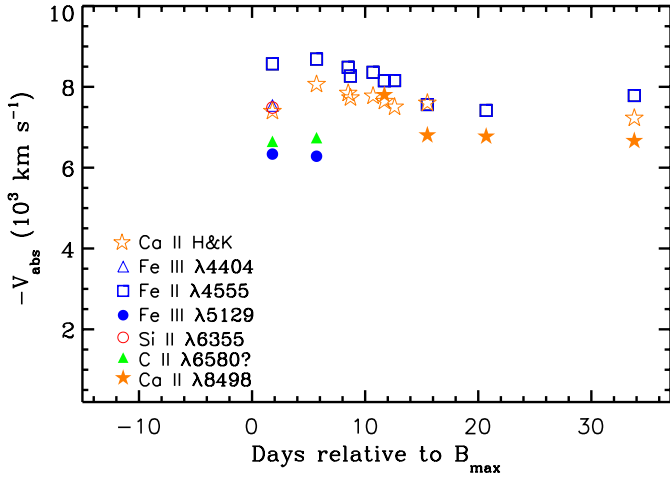[4] In the reference model adopted in this paper $\alpha = 1.22$.

Fig. 9. Evolution of the Doppler velocity at maximum absorption of several prominent ions in the spectra of SN 2012Z. The C II feature is not prominent in the observed spectra and the line identification is suspect. Hence, the inferred velocity is somewhat questionable (see the text for more discussion).

(see Branch et al. 2004, for detailed SYNOW fits to similar epoch spectra of SN 2002cx). Simultaneously, a conspicuous absorption feature attributed to the Ca II NIR triplet emerges, and subsequently grows in strength over the duration of a fortnight. Finally, we note that the near maximum spectra of SN 2012Z shows a weak feature that has been attributed to C II $\lambda6580$ (see Foley et al. 2013, for a discussion).

The NIR spectral time-series of SN 2012Z presented in Fig. 5 contains both the earliest and latest observed epochs of any SN Iax published to date, and therefore provides unique insight into the SN Iax class. Similar to normal SNe Ia observed at very early times, the earliest epoch (−7d) NIR spectrum of SN 2012Z exhibits a rather blue, featureless continuum. Several days later, just prior to maximum the spectrum reveals a shallow feature at wavelengths expected for Mg II $\lambda1.0952\,\mu$m. There is also weak evidence of C I lines at 0.9093, 0.9406, 1.0693 μm, which have been clearly identified in the subluminous Type Ia SN 1999by (Hoeflich et al. 2002). As the SN ejecta expands, the photosphere recedes into the inner regions, resulting in a reduction of the continuum flux, while line features largely associated with Fe-group elements emerge. The evolution of the spectrum and the emergence of Fe-group features tends to occur on a faster timescale in SNe Iax as compared to normal SNe Ia.

Close inspection of the post maximum spectra reveals that by +22d, Co II features dominate the NIR spectrum red-wards of 1.5 μm. This is expected, because Co II features are known to be ubiquitous to the NIR spectra of all other SNe Iax observed to date (see Stritzinger et al. 2014). Turning to the last two observed NIR spectra, minimal evolution of the overall line features is observed to occur between +58d and +269d. Finally, we note that the NIR spectra of SN 2012Z do not exhibit any compelling evidence of spectral features related to He I (White et al. 2014).

The time-evolution of the blue-shifts of a handful of ions present in the early spectra of SN 2012Z were measured in order to estimate the velocity distribution of the emitting regions of the ejecta. The results of which are shown in Fig. 9, and include IME ions of Ca II H&K, Si II $\lambda6355$, C II $\lambda6580$ and Ca II $\lambda8498$, as well as the iron lines Fe II $\lambda4555$ and Fe III $\lambda4404$, $\lambda5129$. The expansion velocity measurements reveal that these ions are related to material with relatively low velocities, all consistently below 10 000 km s^{-1}. Interestingly, at +2d, ions attributed

to Ca II H&K, Fe III $\lambda4404$ and Si II $\lambda6355$ exhibit consistent line velocities of ≈7500 km s^{-1}. This value is bracketed by velocities of Fe II $\lambda4555$ and Fe III $\lambda5129$, which are ∼1000 km s^{-1} higher and lower, respectively. Inspection of Fig. 9 also indicates that at a month past $T(B)_{\max}$ the line velocities evolve rather slowly, with values ranging between 6000 and 8000 km s^{-1}. Taken together the line velocities inferred from the spectroscopic sequence of SN 2012Z suggests a rather low explosion energy compared to normal and over-luminous SNe Ia.

To gain a handle on the radial structure of IMEs in the outer layers of the ejecta, we measured the blue wing velocities in addition to the absorption minima. Blue wings are important since they will not appear if the particular ion does not exist at that velocity. In particular we measured the velocities of the Si II $\lambda6355$ and Mg II $\lambda1.0952\,\mu$m features. Metal lines are not appropriate since even primordial abundances of calcium and beyond can produce background lines. The Si II blue wing is measured to be $v \approx -11\,000$ km s^{-1} on −8d and $v \approx -10\,000$ km s^{-1} on +1.8d, while Mg II is measured with $v \approx -13\,500$ km s^{-1} on −0.4d. These measurements along with the flat evolution of features in velocity space suggests a layered distribution of the IMEs in the outer ejecta (Nomoto et al. 1984). Similar abundance structures have been inferred from the spectral analyses of normal SNe Ia (Jeffery & Branch 1990; Hoeflich et al. 1995; Hoeflich & Khokhlov 1996; Baron et al. 2006; Dessart et al. 2014b), and provides robust constraints on the explosion physics (see below).

4.4. Late phase spectroscopy

The late phase visual-wavelength spectra of SN 2012Z (see Fig. 4) contains nearly a dozen broad emission features, with the majority of cooling occurring through the most prevalent feature centered around ≈7400 Å. This dominant emission feature peaks by a factor of 3 higher in flux than any of the other emission feature, and has a full-width-half-maximum (FWHM) velocity ∼10 000 km s^{-1}. For comparison the weaker emission features exhibit FWHM values between 5700 to 9000 km s^{-1}. Based on similar epoch spectra of other SNe Iax that have lower ejecta velocities, we attribute the ≈7400 Å feature to a blend of a handful of lines, including [Ca II] $\lambda\lambda7291, 7324$ and [Fe II] $\lambda7155$. Foley et al. (2013) reported that *some* SNe Iax exhibit [Ni II] $\lambda7378$ and [Fe II] $\lambda7453$; unfortunately in SN 2012Z the significant blending of features in this wavelength range prevents simple line identifications and therefore, it is not straightforward to determine if these lines are present. Other notable features in the late phase spectra located at ∼5200 Å and 5400 Å are likely produced by the blending of numerous permitted Fe II lines, which have been identified in other SN Iax (Jha et al. 2006; Foley et al. 2013). The emission feature at ≈5900 Å is likely formed from Na I D, while at ≈8300 Å we find features which are more than likely formed by the Ca II NIR triplet. The NIR triplet is commonly seen in SNe Ia and other supernovae, and is strong even at solar abundances.

An alternative identification of the 5900 Å feature could be [Co III] $\lambda5888$ (Dessart et al. 2014a). We note that we find a blend of [Co III] $\lambda5890$, and contributions of [Co III] $\lambda5908$ and [Fe II] $\lambda5872$ in our reference model, but much weaker than observed (see Sect. 5.3).

Beyond these prevalent features, the late phase spectrum of SN 2012Z contain a multitude of low amplitude and low velocity (500–1000 km s^{-1}) features. These features appear to be generic to the SNe Iax class, and have been linked to both forbidden
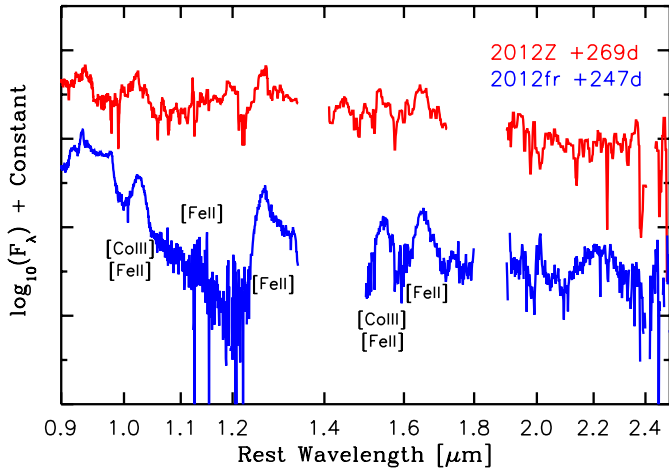
Fig. 10. Comparison of similar epoch late phase NIR spectrum of the normal Type Ia SN 2012fr and the Type Iax SN 2012Z.

and allowed transitions of iron (Jha et al. 2006; McCully et al. 2014a).

We now turn to the examination of the late phase NIR spectrum of SN 2012Z, which to date, is the first of its kind obtained for a SN Iax. Plotted in Fig. 10 is the comparison between our late phase (+269d) NIR spectrum of SN 2012Z, and a similar epoch spectrum of the normal Type Ia SN 2012fr. Clearly, SN 2012Z exhibits many of the same broad features as is seen in the normal SN Ia, particularly at the wavelength regions that correspond to the J and H passbands. Overall, the similarity between the two spectra is quite striking considering the discrepancy between the late phase visual-wavelength spectra between SN 2012Z and other SNe Iax in general, compared to normal SNe Ia (see Fig. 11). Close inspection of the late phase NIR spectrum, albeit of low signal-to-noise, indicates that the [Fe II] $\lambda 1.64$ μm feature has a pot-bellied profile rather than a peaked profile[5]. Similar features have been previously observed in a handful of normal SNe Ia (Hoeflich et al. 2004; Motohara et al. 2006), and as we discuss below, is a signature of high density burning.

5. Bridging observations to model calculations

In the subsequent section, we use the various observational properties of SN 2012Z described in the previous section as a guide to argue that the progenitor is consistent with the theoretical expectations of a pulsating delayed detonation (PPD) explosion of a Chandrasekhar mass ($M_{\rm Ch}$) WD. To do so, we rely upon existing explosion models and link together model predictions to the various observables including amongst others: (1) the light curve properties; (2) the layered structure of the ejecta and; (3) the pot-bellied [Fe II] 1.64 μm profile. The various lines of reasoning are then connected and summarized in Sect. 7 to provide a progenitor scenario to explain at least some SNe Iax.

---

[5] There is confusion in community in the nomenclature to describe central line profiles. Line profiles from constant emissivity shells which are truly flat-topped have been called by the same name as those due to a nickel hole where energy input from γ rays and positrons causes the emissivity to vary. While flat-topped has previously been used in the literature, we want to avoid the confusion between the description of truly flat-topped shell emission that is used to describe optically thin line profiles in a moving shell (Owocki & Cohen 2001) and the profiles we are discussing here, which we refer to as pot-bellied.
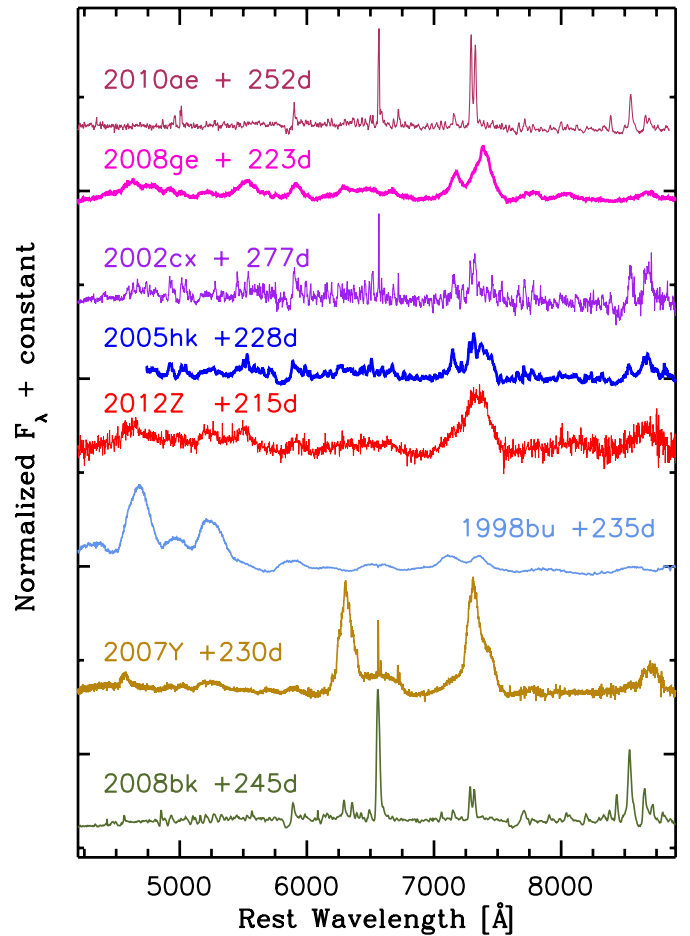
Fig. 11. Comparison of late phase visual-wavelength spectra of a number of SNe Iax and other SN types. The first 5 spectra, sorted from faintest to brightest (*top to bottom*), are the Type Iax SNe 2010ae (Stritzinger et al. 2014), 2008ge (Foley et al. 2010), 2002cx (Jha et al. 2006), 2005hk (Sahu et al. 2008), and 2012Z. Also shown are similar epoch spectra of the normal Type Ia SN 1998bu (Silverman et al. 2013), the Type Ib SN 2007Y (Stritzinger et al. 2009), and the subluminous Type IIP SN 2008bk (Stritzinger et al. 2014). We note in SN 2008bk Balmer lines are associated with emission from the SN ejecta, rather than with the narrower lines associated with host nebular lines, as is the case for SNe 2002cx and 2010ae.

5.1. Interpreting the broadband emission through model comparison

SNe Ia explosions produce a form of stellar amnesia (Hoeflich 2006) and consequently, most explosion scenarios produce very similar structures, ranging from classical deflagration models like W7 to the inner structures of merger (Nomoto et al. 1984; Benz et al. 1990; Livio 1989; Khokhlov 1991; Yamaoka et al. 1992; Hoeflich & Khokhlov 1996; Lorén-Aguilar et al. 2009; Gamezo et al. 2003, 2005; Röpke et al. 2007; Seitenzahl et al. 2009; Pakmor et al. 2011). The abundance distributions reflect the conditions under which burning takes place and therefore exhibit the imprint of the detailed physics that we discuss below. Delayed detonation models (DDT) give the overall chemical stratification where the burning propagates as a deflagration front and then transitions into a detonation (Khokhlov 1991; Yamaoka et al. 1992). Within the DDT scenarios there are two realizations: (1) the WD becomes unbound during the deflagration phase (these are the DD models) and; (2) the WD remains bound at the end of the deflagration phase, then undergoes a

pulsation followed by a delayed detonation transition. This second scenario is called a pulsational delayed detonation (PDD). These two realizations form a sequence which merge at the regime where the WD just becomes unbound. In what follows a classical DD model is used as reference, as well as a PDD model with a large amplitude pulsation to span the range (Hoeflich et al. 1995; Hoeflich & Khokhlov 1996). Beyond our own past work on PPD models, we note that Dessart et al. (2014b) have recently presented a suite of PDD models that cover the range of observed SNe Ia luminosities. Their results are similar to those of Hoeflich et al. (1995); Hoeflich & Khokhlov (1996), and show that PDDs can encompass a wide variety of SNe Ia conditions.

We identified a set of simulations based on the spherical explosion of a M_{Ch} WD, which inherently suppresses mixing. One particular simulation within a series of DD models was identified to exhibit the approximately correct brightness of SN 2012Z. This particular simulation, designated 5p0z22.16 (Hoeflich et al. 2002) is a DD model in which a subsonic deflagration burning front turns into a supersonic detonation wave and mixing in the deflagration phase is suppressed. The 5p0z22.16 simulation gives $[M_B, (B - V)_{max}, \Delta m_{15}(B), \Delta m_{15}(V)]$ of $[-18.22, 0.14, 1.54, 0.99]$, which compares well to $[-18.00, 0.07, 1.62, 0.92]$ and $[-18.27, 0.01, 1.43, 0.89]$ for SN 2005hk and SN 2012Z, respectively. In addition, the model has total and ^{56}Ni masses of 1.362 $M_\odot$ and 0.268 $M_\odot$, respectively, an explosion energy of 1.21×10^{51} ergs, and also produces light curves where the primary and secondary NIR maxima merge into a single maximum (Hoeflich et al. 1995, 2002).

From the observed light curves, M_{Ch} models are consistent with SN 2012Z within the uncertainties of $\approx$10% for different progenitors and $\approx$20% for different explosion scenarios (Hoeflich & Khokhlov 1996; Hoeflich et al. 2013, and references therein). However, in 5p0z22.16 the photosphere recedes from a velocity of about 13 000 km s^{-1} on $-$10d to about 9000 km s^{-1} by maximum light, which is too high compared to what is observed in SN 2012Z. Light curves capture the diffusion timescales of the energy production, but, as discussed below, it takes line profiles to probe the velocity distribution of the elements to understand the nature of SNe Iax.

5.2. Constraints from early phase spectroscopy

In what follows 5p0z22.16 is used as a reference model, but we must consider variations from it that can explain the features of SNe Iax in general, and SN 2012Z in particular. Namely, the model predictions of the photospheric velocities must match the observations. Although this model is a classical DD model, we can think of it as the first in a series of PDD models (Hoeflich et al. 1995), but with a shell mass of zero. Below we consider the effects of variations on the shell mass and how this allows us to subdue the photospheric velocities to match those observed in SN 2012Z. We will be guided in our considerations by the results shown in Fig. 10 of Quimby et al. (2007). Given the low density in the shell some of the original WD's carbon and oxygen (C+O) remains completely unburned in the outer layers. This is in distinction to the classical DD model where all of the material undergoes at least carbon burning.

Early-time spectra can be used to probe the decoupling region of the photons and give a unique measure of the velocity distribution of the elements. Thus, spectral observations probe the density under which burning took place. In velocity space, the 5p0z22.16 simulation (see Fig. 3 in Hoeflich et al. 2002) shows products of explosive carbon burning, namely oxygen and magnesium, incomplete

oxygen burning, that is silicon and sulphur, and complete burning close to nuclear statistical equilibrium (NSE), i.e. iron/cobalt/nickel (Fe/Co/Ni), in the velocity ranges of [13 000–18 000], [7000–14 000] and [0–6000] km s^{-1}, respectively. An inner region of about 3000 km s^{-1} shows elements of stable isotopes of Fe/Co/Ni due to electron capture, a signature of high-density, M_{Ch} models. Calcium is produced in the range [5000–13 000] km s^{-1}, and is destroyed at lower velocities.

In the standard DD scenario for subluminous SNe Ia, specifically model 5p0z22.16, deflagration burning with mixing during the deflagration suppressed, only burns material up to velocities of about 4300 km s^{-1} (see e.g., Fig. 1 in Hoeflich et al. 2002). SN 2012Z shows Fe-group elements up to, at least, 9000 km s^{-1} (Fig. 9), which is some 3000 km s^{-1} higher than where ^{56}Ni is produced during the detonation phase of the reference model. Fe-group elements are formed during high density burning beyond $1-2 \times 10^7$ g cm^{-3}, strongly suggesting mixing in a M_{Ch} scenarios, or an increase in production of ^{56}Ni during the detonation phase.

An increased production of ^{56}Ni within the classical-detonation scenario would lead to an even more extended region of IMEs than 5p0z22.16, which is inconsistent with SN 2012Z. Detonations in smooth density structures will unavoidably produce extended distributions of IMEs in velocity space or if the density is high, hardly any production of IMEs. Because the specific energy production depends on the nuclear processes, the latter case would also produce high velocity ^{56}Ni (Khokhlov et al. 1993; Hoeflich & Khokhlov 1996). We note that the same arguments would apply to sub-M_{Ch} explosions triggered by the ignition of an outer helium layer (Woosley et al. 1980; Nomoto 1982; Woosley & Weaver 1994; Hoeflich & Khokhlov 1996; Nugent et al. 1997; Sim et al. 2012).

Mixing may occur both during the deflagration phase of burning and during a pulsation phase of the WD prior to the initiation of the detonation, while the detonation phase leads to a layered structure. During the last decade, significant progress has been made in our understanding of the deflagration phase. On a microscopic scale, a deflagration propagates because of heat conduction by electrons. However, all current simulations have found burning fronts to be Rayleigh-Taylor (RT) unstable increasing the effective burning speed, predicting homogeneous mixing of products of incomplete and complete burning (Livne & Arnett 1993; Livne 1993; Khokhlov 1995; Gamezo et al. 2003; Reinecke et al. 2002; Gamezo et al. 2005; Röpke et al. 2007; Seitenzahl et al. 2009, 2013). As seen in Fig. 9, mixing of IMEs and calcium is not observed in SN 2012Z at velocities less than $\approx$6500 km s^{-1}. Ca II is commonly seen in SNe Ia even in the outer layers, that at most undergo carbon burning at solar metallicities (see for example Lentz et al. 2000), arguing against mixing of the inner layers during a deflagration burning phase.

Both mixing and an upper limit for the distribution of burning products can be understood in terms of models that undergo a pulsational phase prior to the detonation (Khokhlov et al. 1993; Hoeflich et al. 2004; Hoeflich & Khokhlov 1996; Livne 1999; Livne et al. 2005; Quimby et al. 2007; Dessart et al. 2014b). In this class of PDD models, a M_{Ch} WD remains bound after the deflagration phase. The deflagration mostly produces Fe-peak isotopes; subsequently, an extended envelope is formed. As the explosion progresses, and the bound shell falls back a detonation is triggered that leads to the production of IMEs and a massive shell. The mass of the shell determines the upper velocity limit of the burning products (Khokhlov et al. 1993; Hoeflich & Khokhlov 1996; Quimby et al. 2007). To be aligned with

SN 2012Z's measured blue wing velocity of Si II (see Sect. 4.3), a shell mass of $\approx$0.05–0.12 $M_\odot$ is required (see Fig. 10 in Quimby et al. 2007). In addition the blue wing velocity of Mg II is consistent with a shell mass of $\sim$0.08 $M_\odot$. Early multidimensional calculations indicated that WDs become unbound during the deflagration phase (Gamezo et al. 2003; Röpke et al. 2007), but this conclusion depends sensitively on the assumption for the thermonuclear runaway (Livne et al. 2005). This strong dependency on the basically unknown initial conditions of the WD is an obstacle for fitting details of a specific supernova, but is consistent for the wide variety of properties displayed by SNe Iax.

It is well known that weak interaction/pulsation or the presence of a low-mass buffer around the exploding white dwarf can dramatically alter the outer ejecta layers of the SN Ia explosion (Hoeflich et al. 1995; Hoeflich & Khokhlov 1996; Dessart et al. 2014b). The specific properties of the pulsation can affect the appearance of C I, C II, and O II lines The presence or absence of C I, C II and O II is also sensitive to the details of the excitation. Some realizations within PDD and DD models do in fact show strong optical and NIR C I and C II lines (Hoeflich et al. 2002; Dessart et al. 2014b). However, C II λ6580 lines at velocities as $\sim$7000 km s^{-1} (Fig. 9) is somewhat in contradiction with also weak C I λ1.0694 μm in the NIR at higher velocity ($\sim$10 000 km s^{-1}). Alternative identifications for the optical feature are due to lines of Co II and Si II.

We note that in PDDs there can be extra energy left over from shock heating in the unburned regions with may lead to higher temperatures than in classical DD models (Dessart et al. 2014b). Some energy from interaction may also lead to higher temperatures and hotter spectra (Gerardy et al. 2004). Mixing of radioactive material through the C+O region is disfavored as we have already discussed above.

5.3. Late phase spectroscopy

Independent of the details of the explosion scenario the inner regions of SNe Ia ejecta are quite similar. Modulations due to variations in PDD models do not affect the bulk of the inner regions of the ejecta for models that produce the same amount of ^{56}Ni (Hoeflich et al. 1995; Hoeflich & Khokhlov 1996; Dessart et al. 2014b). As discussed above we can probe the ^{56}Ni distribution using our reference model.

5.3.1. Methods

Calculations of explosions, light curves, and spectra are performed using the HYDro RAdiation transport (HYDRA) code (Hoeflich 1990; Hoflich 1995; Hoeflich 2003, 2009a). HYDRA solves the hydrodynamics using the explicit Piecewise Parabolic Method (PPM; Colella & Woodward 1984), detailed nuclear and atomic networks (Cyburt et al. 2010; Kurucz 1994; Hoflich 1995; Seaton 2005), radiation transport including γ rays and positrons by variable Eddington Tensor solvers and Monte Carlo Methods (Mihalas & Mihalas 1984; Stone et al. 1992; Hoeflich 2003; Hoeflich et al. 1993; Hoeflich 2009b; Penney 2011). For this study, forbidden line transitions have been updated using the atomic data in De et al. (2010a,b), Friesen et al. (2014), and The Atomic Line List V2.05B18[6] by Peter van Hoof. For the overall evolution, we use simplified atomic models limited to about 2000–10 000 discrete levels using level merging or superlevels (Anderson 1989; Dreizler & Werner 1993; Hubeny & Lanz 1995; Schweitzer et al. 2000; Hillier 2003; Hoeflich 2003, 2009a). To compute NIR line profiles, we do not use superlevels

---

[6] At http://www.pa.uky.edu/~peter/newpage/

but calculate the emission by postprocessing of the background model (Hoeflich et al. 2004; Penney 2011; Sadler et al. 2012; Hoeflich et al. 2013). Nevertheless, line ratios and excitation state depend sensitively on collisional de-excitation – uncertainties in the collisional cross sections have been and continue to be the main uncertainies in determining the level populations (Axelrod 1980; Bowers et al. 1997; Liu et al. 1997; Gerardy et al. 2007).

5.3.2. Spectral analysis

All thermonuclear explosion models show centrally peaked density profiles, therefore at late times, due to simple geometrical dilution line formation should occur closer to the center at lower velocities yielding narrow line profiles. In fact, if we see to the center the line profile should peak at zero velocity because of the central caustic. However, because of the mass-radius relation of WDs, lower mass progenitors will have significantly lower central densities. If the central density becomes very low, such as in a sub-Chandrasekhar detonation or merger, than calcium will not be burned at low velocity, as noted above.

The low velocity Fe-group material seen in the late phase visual-wavelength spectra are a natural result of the PDD scenario, but can also be explained by pure deflagration models that produce very low energy explosions (see, for example Reinecke et al. 2002), as well as by deflagrations leaving bound remnants (Kromer et al. 2013; Fink et al. 2013), and merger models (Piersanti et al. 2003; Pakmor et al. 2011).

Late phase spectra beyond 200 days are dominated by forbidden emission lines which are powered by positrons originating from the β^+ decay of ^{56}Co. At this phase, hard γ rays from the decay escape for all classes of explosion scenarios (Hoeflich et al. 1992). Up to about one year after the explosion, the mean free path of positrons is small, leading to local energy deposition and excitation of levels (Milne et al. 2002; Penney 2011; Sadler et al. 2012), which traces the initial ^{56}Ni distribution. Thus, emission line profiles at optical and NIR wavelengths traces the ^{56}Ni distribution in velocity space, though blends may broaden the features and affect the details of the line profiles, particularly in the optical.

NIR spectra at late epochs of normal SNe Ia are dominated by blended forbidden lines of [Fe I], [Fe II], [Fe III], [Co II] and [Co III] (Hoeflich et al. 2004; Motohara et al. 2006). As normal SNe Ia evolve in time, the strengths of their NIR spectral features change due to the ionization state of the line forming regions, which is linked to the ever decreasing decay of ^{56}Co. During this time the 1.5–1.7 μm region is dominated by a multitude of blended forbidden [Fe II] and [Co III] lines, with major contributions attributed to [Fe II] $\lambda\lambda$1.53, 1.64, 1.67 μm, and [Co III] λ1.55 and λ1.76 μm (Hoeflich et al. 2004). Eventually, the IR-catastrophe (Fransson et al. 1994) is expected to cause a redistribution of the energy deposition to the NIR and beyond, however light curve observations of SNe Ia constrain this possible phase to much later epochs than considered in this paper (Sollerman et al. 2004; Strizinger & Sollerman 2007; Leloudas et al. 2009; McCully et al. 2014a).

Figure 12 shows the comparison between the +215d optical (left panel) and +269d NIR (right panel) spectra of SN 2012Z compared to the +220d reference model. As discussed above, the spectra are dominated by single and doubly ionized lines of iron group elements, with almost all of the optical features formed from blends of various species. Many of the more prevalent observed features are reproduced by the synthetic spectrum, however some discrepancies are apparent. The
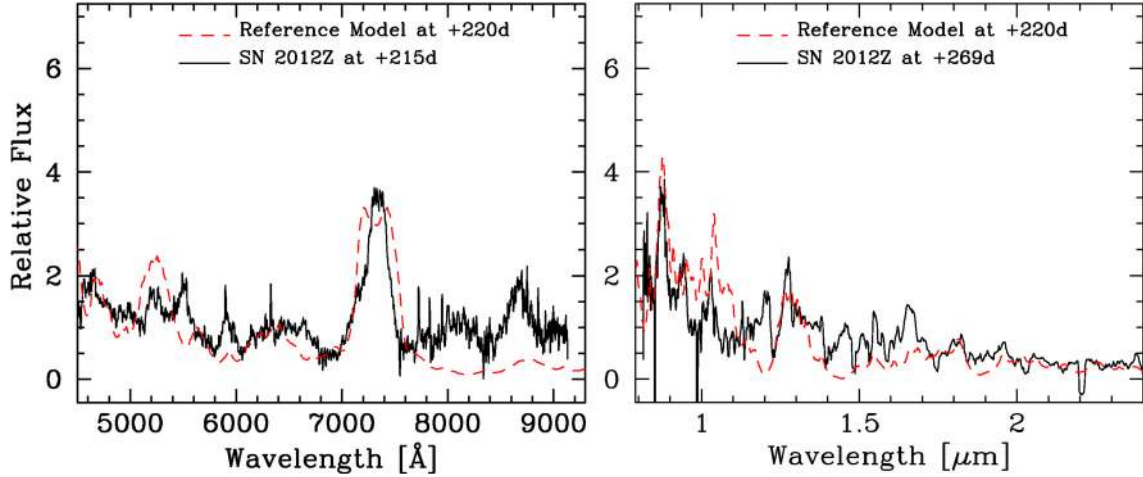
Fig. 12. Late phase optical (*right*) and NIR (*right*) spectrum of SN 2012Z compared to the synthetic spectrum computed from the reference model.

prominent ~7400 Å feature is well-matched by the synthetic spectrum. However, the observed feature is slightly asymmetric on the blue wing, whereas the synthetic feature shows multiple components formed by [Ca II] $\lambda7325.9$, [Fe II] $\lambda\lambda7390.2$, 7454.6 7639.6, with a significant contribution from [Ni II] $\lambda\lambda7379.9$, 7413.6. Here [Ca II] contributes significantly to the line width of the blue wing. The blue features are too strong in the synthetic spectrum, which is likely due to inaccuracies in the atomic data and the use of superlevels.

Other notable features are found to be formed by [Fe III] $\lambda\lambda4659.5$, 4703.0, 4735.3, 4770.9, [Fe III] $\lambda\lambda4932.0$, 5012.8, [Fe II] $\lambda5113.1$, [Fe II] $\lambda5160.2$, [Fe II] $\lambda\lambda5221.5$, 5263.1, [Fe III] $\lambda5272.0$, [Fe II] $\lambda\lambda5263.1$, 5298.3, [Fe II] $\lambda\lambda5335.1$, 5377.9, [Co III] $\lambda\lambda5890.1$, 5908.4 blended with [Fe II] $\lambda5872$, [Co III] $\lambda6578.1$, [Ni II] $\lambda6668.6$, and [Co III] $\lambda6855.4$ blended with [Fe II] $\lambda\lambda6875.7$, 6898.1.

In addition, we see [Fe II] $\lambda8619.3$ and [Fe III] $\lambda\lambda8840.6$, 9036.0 though it appears slightly too low, most likely due to discrepancies in the atomic line data. [C I] $\lambda8729.5$ may contributes to the observed feature at ~8600 Å; however, in the reference model, it forms at too high a velocity and is not the dominant transition. Another interesting feature present in both the models and SN 2012Z is the [O I] $\lambda\lambda6302.0$, 6302.0, 6393.5 triplet, which appears rather weak. The weak oxygen excitation expected in both DD and PDD models is due to the separation of ^{56}Ni and the region of explosive oxygen burning (that is where silicon and sulfur are formed), if mixing in the PDD scenario remains limited to a region smaller than the Si/S shell, as it appears to be in SN 2012Z.

The NIR synthetic spectrum of Fig. 12 also shows a host of [Fe II] and [Fe III] lines as seen in the optical. Specifically showing features at 0.95, 1.25, 1.5, 1.6, 1.8 μm, including the strong feature at 1.25 μm which is a blend of [Fe II], [Fe III] and [Ni II]. An interesting feature located ~1.032 μm is attributed to a multiplet of [S I]. Even moderate microscopic mixing of ^{56}Ni would highly excite the levels of [S I] producing a very prominent feature. Even higher excitation, due to more mixing would produce a strong [S II] feature at $1.02-1.04$ μm[7].

It is well established that the late-time NIR line profiles of [Fe II] features trace the energy input by radioactive decay (Hoeflich et al. 2004; Motohara et al. 2006; Maeda et al. 2010). Because of the structure of the atomic levels, the relatively

---

[7] Microscopic means on scales smaller than the mean free path for positrons (Hoeflich et al. 2002; Penney 2014).
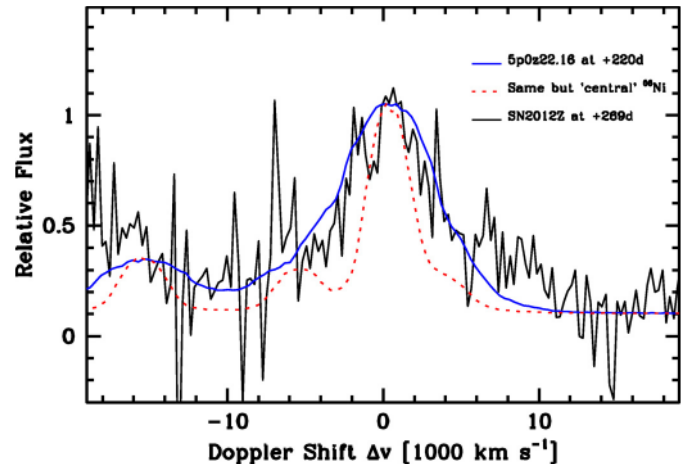
Fig. 13. Effect of the ^{56}Ni distribution upon the late phase [Fe II] $\lambda1.64$ μm feature. Comparison of this feature from the +269d spectrum of SN 2012Z (black) to the expected line profile computed from the 5p0z22.16 model at +220d for two different ^{56}Ni distribution. Plotted in blue is the synthetic spectra for the original model which has a hole in the ^{56}Ni distribution of ≈3000 km s^{-1}, while in red is the synthetic spectrum with ^{56}Ni concentrated in the center.

unblended [Fe II] 1.64 μm line is a particularly good tracer of the inner region. In a handful of the SNe Ia observed several hundred days past maximum, NIR emission lines have been found to exhibit pot-bellied profiles. This observational characteristic is the hallmark of M_{Ch} WD progenitors that explode with high central densities, of the order $\lesssim 10^9$ g cm^{-3} (Hoeflich et al. 2004; Motohara et al. 2006; Hoeflich et al. 2006; Fesen et al. 2007; Gerardy et al. 2007; Maeda et al. 2010; Hoeflich et al. 2013). At masses close to the M_{Ch}, central densities can become sufficiently high that electron capture processes shift the NSE distribution to stable isotopes of Fe/Co/Ni, leaving a ^{56}Ni hole at the center of the supernova ejecta, and thereby generate the pot-bellied profiles. This produces a central hole in ^{56}Ni of about 3000 km s^{-1} without mixing, very similar to SN 2003du and SN 2003hv (Hoeflich et al. 2004; Motohara et al. 2006). As pointed out in Sect. 4.4, the [Fe II] $\lambda1.64$ μm feature of SN 2012Z also exhibits a pot-bellied profile (see Fig. 10), providing an additional indication that its progenitor was at or near the M_{Ch}.

For clarity on this point, in Fig. 13, we show the effect of the ^{56}Ni distribution on the late phase (+269d) [Fe II] $\lambda1.64$ μm line profile. Here the observed feature (black line) is compared
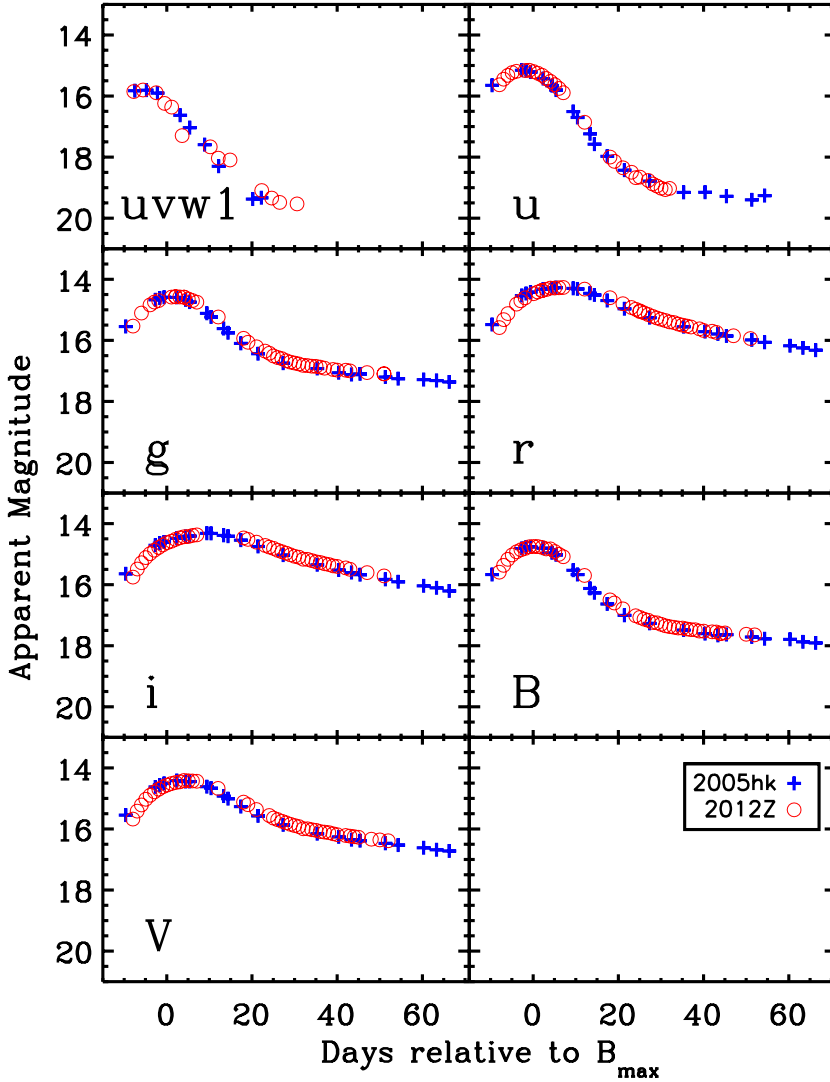
Fig. 14. Comparison of *uvw*1- and *ugriBV*-band light curves of SNe 2005hk (black plus symbols) and 2012Z (red circles). The light curves of SN 2005hk have been shifted to match the peak magnitudes of SN 2012Z.

to the model calculations of 5p0z22.16 at +220d for two cases: (1) a hole in the ^{56}Ni distribution of ∼3000 km s^{-1} (blue line) and; (2) with the ^{56}Ni placed at the center of the ejecta (red line). A magnetic field of 10^6 G has been assumed. The blue line is clearly pot-bellied, as in the case of subluminous SNe Ia at the same epoch, because some ≈6% of all γ rays excite the high density, central region (Hoeflich et al. 1991, 2002).

The case for a M_{Ch} explosion is quite strong, lower initial WD masses would produce ^{56}Ni confined to the central regions, due to the lower densities in lower mass WDs. More centrally confined ^{56}Ni would have longer diffusion times, thus falling closer to the the light-curve brightness decline-rate relation and it would not produce the observed spectra since the longer diffusion times would lead to cooler (redder) light curves and spectra more similar to fast decliners like SN 1991bg. Moreover, the persistent pot-bellied line profiles in the NIR require high densities only found in M_{Ch} explosions.

6. Further comparison between SN 2005hk and SN 2012Z

In this section we further explore the commonalities between the observational properties of SNe 2005hk and 2012Z. The former of these objects is a well-observed SN Iax that has been previously documented to be similar to the prototypical Type Iax

SN 2002cx (Phillips et al. 2007; Sahu et al. 2008). As previously highlighted, SNe 2005hk and 2012Z exhibit comparable decline-rate values (Fig. 6), color curves (Fig. 7), and peak luminosity (Fig. 8). We now proceed to compare the shape of their light curves, and their optical and NIR spectra at various epochs.

Plotted in Fig. 14 is the comparison of the *uvw*1- and *ugriBV*-band light curves of both supernova plotted vs. $T(B)_{max}$, where the filtered light curves of SN 2005hk have been shifted to match the peak magnitudes of SN 2012Z. Overall the shape of the optical light curves are exceedingly similar, with perhaps the only subtle difference being that SN 2012Z appears to rise to maximum brightness at a slightly faster rate. This is consistent with the ^{56}Ni being distributed somewhat closer to the surface, leading to shorter diffusion times.

Figure 15 is a comparison between the −8d, +2d and +21d visual-wavelength spectra of SN 2012Z, and similar epoch spectra of SN 2005hk (Phillips et al. 2007). Overall the two objects are remarkably similar, exhibiting similar continua, and nearly identical spectral features at all epochs. Comparing the expansion velocities of SN 2005hk (see Phillips et al. 2007, their Fig. 9) and SN 2012Z (see Fig. 9), shows that the latter consistently exhibits v_{exp} values which are about 1500 km s^{-1} higher for all ions. The similar magnitude v_{exp} values between the two events is indicative that they had comparable explosion energies, while the broader line widths observed in SN 2012Z can
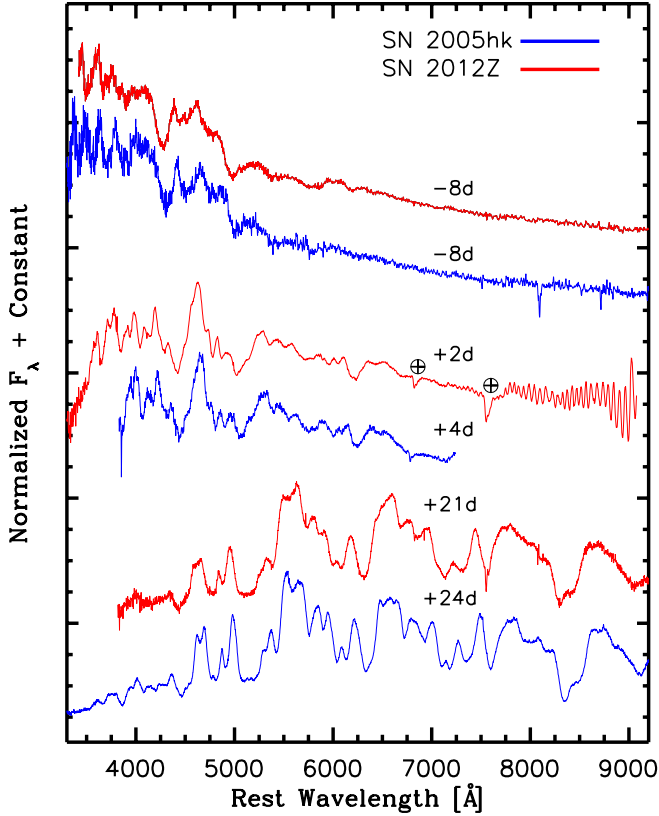
Fig. 15. Comparison of visual-wavelength spectra of SN 2012Z at phases of −8d, +2d, and +24d to similar epoch spectra of SN 2005hk (Phillips et al. 2007).

Fig. 16. Comparison of NIR-wavelength spectra of SN 2012Z at phases of 0d (*top*) and +22d (*bottom*), to similar epoch spectra of SN 2005hk (Kromer et al. 2013). Prevalent features attributed to ions of Fe II, Si III, and Co II are indicated with labels.

be attributed to an optical depth effect caused by its ^{56}Ni distribution extending to higher velocities. This suggests that the ^{56}Ni was produced in different regions in SN 2005hk and SN 2012Z, implying that the explosion mechanism varied either due to some variation in a violent merger or more likely, that they both occurred due to a PDD explosion (Khokhlov 1991; Khokhlov et al. 1993; Hoeflich & Khokhlov 1996), where the mass of the pulsational shell varied leading to ^{56}Ni production closer to the center in SN 2005hk and further out in SN 2012Z. Thus, we can think of the variation between SN 2005hk and SN 2012Z as variations in the kinetic energy of the ^{56}Ni, and not variations in the total kinetic energy of the explosion.

Figure 16 shows a comparison between the NIR spectrum of SN 2012Z obtained at maximum (top panel) and three weeks later (bottom panel) to similar epoch spectra of SN 2005hk (Kromer et al. 2013). At both epochs the spectra of the two objects are very similar, with the main difference again being the moderately higher blueshifts of the absorption features in SN 2012Z. Another noticeable difference observed in the bottom panel is that the strength of many of the absorption features appears stronger in SN 2005hk, particularly the [Co II] lines located between ≈1.6–1.8 μm. This is due to the Fe-group elements in SN 2005hk being slightly more confined in velocity space. In fact, all of the line profiles are somewhat more confined in velocity space due to the more central nickel distribution in SN 2005hk.

7. Discussion

From the findings presented in the previous sections it is clear that SN 2012Z is among the brightest and most energetic SN Iax

yet observed, extending the parameter space of this peculiar class of transients. It is also apparent that objects populating the bright end of the SN Iax luminosity distribution exhibit exceedingly similar observational parameters. In Sect. 4.2 we derived explosion parameters based on a number of underlying assumptions that provide model fits to the UVOIR light curves of SNe 2005hk and 2012Z. The model fits suggest ^{56}Ni values ranging between 0.2–0.3 $M_\odot$, E_K values of ≈10^{51} erg, and ejecta masses consistent with M_{Ch}.

We have presented a possible explosion scenario that explains the nature of at least some SNe Iax. This involves a PDD explosion of a near M_{Ch} WD. The production of Fe-group elements occurs in the deflagration phase (in distinction to normal SNe Ia where the Fe-group elements are primarily produced in the detonation phase, leading to a more layered or radially stratified structure). Our scenario explains both the photospheric velocities of the IMEs, as well as the high densities required by the late phase NIR spectra. The production of ^{56}Ni closer to the photosphere also simply explains the blue colors and hot spectra. From our reference model and the series of PDD models of Hoeflich et al. (1995) we would find the total mass of ^{56}Ni to be ≈0.2 $M_\odot$.

SN 2012Z provides a uniquely large data set which allows a detailed analysis covering a wide range of observables unparalleled even for typical SNe Ia. The nature of SN 2012Z is a theoretical challenge, because several important physics aspects in thermonuclear explosions are not well understood, such as: the progenitor evolution; the thermonuclear runaway; rotation; and so on, making fully self consistent models a goal for the future. These problems lead to the wide variety of models suggested for SNe Iax.

Using both analytic and numerical models as benchmarks, we were able to develop constraints for SN 2012Z based on multiple observables. The light curves suggest a massive, close to M_{Ch}, WD as the progenitor. From the peak brightness we may estimate the mass to be within ~0.2 $M_\odot$ of M_{Ch}. This view is supported by the pot-bellied, late-time NIR line profiles that can be understood by high-density burning taking place at densities in excess of 10^9 g cm^{-3}, which puts the progenitor within about 0.02 $M_\odot$ of the M_{Ch}. The other, less stringent constraint, $M > 1.2$ $M_\odot$, is from the lack of Ca II (and other IMEs) at low velocities, which even at solar abundance, produces very strong features in the optical and NIR. Thus, solar abundance primordial calcium must have been burned at low velocities.

Light curves are mostly determined by diffusion timescales, that is, their appearance is dictated by the nature of the innermost regions. The light curve rise time is determined by the nickel distribution. Even with M_{Ch} progenitors, fast rise times and slow declines can be reproduced (Baron et al. 2012). Within this model elements produced in the deflagration will be mixed, while those produced in the detonation will have a layered structure. We note that the detonation running through the material previously burned in the deflagration will reproduce the layered structure.

PDDs are similar to deflagrations, but have a detonation phase which produces a layered structure without requiring a bound remnant. Because PDD models may vary in the ratio of energy released to binding energy (Quimby et al. 2007) they produce a wide range of ^{56}Ni masses. Since the shell mass may vary, a range of unburned C+O in the outer layers can also be in PDDs.

The similarity between SN 2012Z and SN 2005hk suggests very similar properties of the exploding WDs. However, SN 2012Z has undergone relatively enhanced mixing to bring Fe-group elements to the base of the incomplete oxygen burning (Si/S) region. All multidimensional models predict mixing by RT instabilities which produce an almost homogeneous mixing of the layers of IMEs with those below. In SN 2012Z, we see a layered structure, the signature of detonations, for calcium, silicon, and magnesium. This suggests that these elements are produced in a detonation phase after the mixing has occurred and the majority of Fe-group elements have been synthesized. RT instabilities in the deflagration phase seem to be a stable feature from the hydrodynamical view making deflagration models much less favorable as compared to models that result in the layered structure observed in SNe Ia. Detonation fronts in a WD will produce IMEs in a wide velocity range due to the smooth density structure and thus, slowly varying burning conditions. An exception to this picture can be found in the PDD models, where low densities in an shell prevent burning to the Fe-group by a detonation, and limit the expansion velocities of the burning products. For SN 2012Z, we need a shell mass of about 0.05–0.12 $M_\odot$ to be consistent with the low range of velocities observed in IMEs of SN 2012Z. We also need little or no production of ^{56}Ni during the detonation phase. PDDs model will not show signatures of narrow (low velocity) oxygen features at late phases because oxygen is consumed during the detonation phase. Moreover, as the expansion velocities of SNe Iax are roughly half of what is observed in normal SNe Ia, densities are kept sufficiently high to suppress spectra dominated by forbidden lines of Fe-group elements out to eight times later than observed in SNe Ia, or roughly two to three years past explosion.

Because most of the ^{56}Ni production occurs during the deflagration phase, we expect a wide variation in the Δm_{15} relation compared to normal SNe Ia in which most of the ^{56}Ni is produced during the detonation phase. This is due to the fact that the amount of ^{56}Ni produced and its spatial distribution will depend sensitively on the mixing during the deflagration phase, rather than the smooth layered nickel distribution produced in the detonation phase.

PDD models synthesize abundances of ^{56}Ni that range from near zero to 0.8 $M_\odot$, and therefore offer the flexibility to produce both bright and dim events. While our proposed model seems to do a reasonable job of explaining the moderately bright SN 2005hk and SN 2012Z, and perhaps also the low luminosity SN 2010ae, we should stress the limitations of our analysis. It is not yet clear whether all SNe Iax are a homogeneous class, or like SNe Ia, will show wide variations. Our analysis here has only been a qualitative description of our scenario. To understand how widely applicable it is to SNe Iax as a class a detailed parameter study with radiative transfer needs to be compared to large data sets of individual SNe Iax.

A common problem with both the PDD model and models with C+O shells, depending on the mass and the amplitude of the explosion, may be the optical depth of the shell during early times which could lead to high velocity calcium and other background metal lines. Accretion from a helium or low metallicity star may reduce this problem due to the low opacity of both unexcited helium (since γ rays are shielded from the surface). If there is a significant unburned C+O shell then CO molecules may form which would provide an important coolant and should be visible in the mid infrared (Hoeflich et al. 1995).

Pure deflagration models have been suggested as a candidate scenario for SNe Iax since they can produce a wide range of kinetic energies, and peak brightnesses (Phillips et al. 2007; Sahu et al. 2008). Depending on the initial conditions, pure deflagrations may or may not leave a bound remnant (Reinecke et al. 2002; Fink et al. 2013). Recently a suite of model calculations has been presented, especially designed for SNe Iax, that consist of C+O WDs that undergo deflagration driven disruption leaving bound remnants (Jordan et al. 2012; Fink et al. 2013; Kromer et al. 2013).

Kromer et al. (2013) presented a pure deflagration model leading to a bound remnant of nearly 1 $M_\odot$, which produces enough ^{56}Ni to account for the peak brightness of SN 2005hk. Their model does a reasonable job of fitting the photospheric phase optical spectral around maximum light, and the fast rise and slow late-time decline of the light curve of SN 2005hk. In this model the remnant serves to explain the absence of late-time oxygen lines that are produced by the incomplete burning and mixing inherent in pure deflagration models.

Any model that involves a pure deflagration will give a non-layered structure with mixing of unburned material, IMEs, and Fe-group elements throughout the entire ejecta. In particular, this would produce low-velocity oxygen lines at late times (Kozma et al. 2005). The model of Kromer et al. (2013) avoids the appearance of low velocity unburned material by leaving the central regions behind in the bound remnant, while not producing a radially stratified ejecta. Late-time spectra of SN 2012Z (see Fig. 11) show shell like line profiles which may be produced in the bound remnant scenario, but the low mass may lead to the formation of true shell-like profiles, that is the formation of horned emission lines. It remains for future calculations to determine if the bound remnant model is able to produce disruptions that synthesize the small amounts of ^{56}Ni measured in the 2008ha/2010ae-like SNe Iax. In the same context, the PDD models that are found in the literature have also not been extended to the dimmest extent in order to be compared with the observations of the faintest members of the SNe Iax class.

In many respects, other models invoking detonations, such as dynamical merging scenarios and helium detonations cannot be ruled out for SNe Iax as they may produce similar configurations as PDD models (Benz et al. 1990; Livio 1989; Lorén-Aguilar et al. 2009; Pakmor et al. 2011; Shen et al. 2010; Ruiter et al. 2014). However, they may also be somewhat disfavored due to the lack of polarization observed in SNe Ia and SNe Iax (Chornock et al. 2006; Maund et al. 2010; Patat et al. 2012). Additionally the late phase spectra of SN 2012Z, seem to disfavor merger models due to lower densities in the progenitors which leads to ^{56}Ni all the way to the center (see Sect. 4.4).

Characteristics in favor of PDD-like models come from the advantages of combining attributes of deflagration and detonation models. As discussed above, the late phase spectra of SN 2012Z show evidence of burning at high densities.

The observational properties described in this paper for SN 2012Z have also not been probed for the majority of SNe Iax, due to incomplete data sets. We note that combining the observed characteristics from different SNe Iax could lead to wrong conclusions. Therefore we cannot exclude that a wide variety of scenarios may be realized within the SNe Iax class.

Understanding the nature of SNe Iax will also come from determinations about the progenitor system in individual cases. McCully et al. (2014b) have observed the progenitor system of SN 2012Z with HST via serendipitous measurements of the host galaxy. They find a stellar source for the progenitor, S1, which is luminous and blue. Examining the color magnitude diagram for S1, it is found that it is consistent with a massive blue supergiant, which is a very unlikely progenitor for SN 2012Z in any scenario. They conclude that they may be seeing the donor companion star, likely a $\sim$2 $M_\odot$ helium star. While the current observations are not completely aligned with our expectations of a hot disk as the source of S1, it is possible that the environment is contaminated enough that at least some of the light from S1 is indeed from the hot accretion disk. Nevertheless, the observed progenitor fits in with a single degenerate explosion which would be consistent with our proposed scenario. More will be learned from future observations of the putative progenitor when the light from the supernova has faded.

In conclusion, we stress that future efforts to model the SN Iax class should aim to provide robust radiative transfer calculations in order to compare to the detailed optical and NIR spectroscopic sequences now being routinely obtained at *both* early and late phases. We have shown that there are constraints that models must obey, but quantitative comparison with the full SNe Iax class requires a wide parameter study of the variety of mixing and pulsation properties. Such a study is underway, and should provide confirmation or not of whether PDD models may indeed provide a viable explosion model for SNe Iax.

References

Anderson, L. S. 1989, ApJ, 339, 558
Arnett, W. D. 1982, ApJ, 253, 785
Axelrod, T. S. 1980, Ph.D. Thesis, Harvard University
Baron, E., Bongard, S., Branch, D., & Hauschildt, P. H. 2006, ApJ, 645, 480
Baron, E., Hoeflich, P., Krisciunas, K., et al. 2012, ApJ, 753, 105
Benz, W. Cameron, A. G. W., Press, W. H., & Bowers, R. L. 1990, ApJ, 348, 647
Bernstein, R. Shectman, S. A., Gunnels, S. M., et al. 2003, Proc. SPIE, 4841, 1694
Bowers, E. J. C., Meikle, W. P. S., Geballe, T. R., et al. 1997, MNRAS, 290, 663
Branch, D. 1992, ApJ, 392, 35
Branch, D., Baron, E., Thomas, R. C., et al. 2004, PASP, 116, 824
Breeveld, A. A., Landsman, W., Holland, S. T., et al. 2011, in Gamma-Ray Bursts 2010, eds. J. E. McEnergy, J. L. Racusin, & N. Gehrels (Melville, NY: AIP), AIP Conf. Proc. 1358, 373
Brown, P. J., Holland, S. T., Immler, S., et al. 2009, AJ, 137, 4517
Brown, P. J., Roming, P. W. A., Milne, P., et al. 2010, ApJ, 721, 1608
Burns, C. R., Stritzinger, M. Phillips, M. M., et al. 2011, AJ, 141, 19
Burrows, D. N., et al. 2005, Space Sci. Rev., 120, 165
Cartier, R., Hamuy, M., Pignata, G., et al. 2014, ApJ, 789, 89
Cenko, S. B., Cohen, D. P., Silverman, J. M., & Ganeshalingam, M. 2012, Central Bureau Electronic Telegrams, 3014, 3
Chornock, R., Filippenko, A. V., Branch, D., et al. 2006, PASP, 118, 722
Colella, P., & Woodward, P. R. 1984, J. Comput. Phys., 54, 174
Colgate, S. A., & McKee, C. 1969, ApJ, 157, 623
Contreras C., Hamuy, M., Phillips, M. M., et al. 2010, AJ, 139, 519
Cyburt, R. H., Amthor, A. M., Ferguson, R., et al. 2010, ApJS, 189, 240
Diamond, T. 2014, Ph.D. Thesis, The Florida State University
De, S., Baron, E., & Hauschildt, P. H. 2010a, MNRAS, 407, 658
De, S., Baron, E., & Hauschildt, P. H. 2010b, MNRAS, 401, 2081
Dessart, L., Hillier, D. J., Blondin, S., & Khokhlov, A. 2014a, MNRAS, 439, 3114
Dessart, L., Blondin, S., Hillier, J. D., & Khokhlov, A. 2014b, MNRAS, 441, 532
Dreizler, S., & Werner, K. 1993, A&A, 278, 199
Fesen, R. A., Hoeflich, P. A., Hamilton, A. J. S., et al. 2007, ApJ, 658, 396
Filippenko, A. V. 2005, in The Fate of the Most Massive Stars, eds. R. Humphreys, & K. Stanek (San Francisco, CA: ASP), ASP Conf. Ser., 332, 33
Filippenko, A. V., Li, W. D., Treffers, R. R., Modjaz, M. 2001, in Small-Telescope Astronomy on Global Scales, eds. W. P. Chen, C. Lemme, & B. Paczynski (San Francisco, CA: ASP), ASP Conf. Ser., 246, 121
Fink, M., Kromer, M., Seitenzahl, I., et al. 2013, MNRAS, 429, 2287
Fitzpatrick, E. L. 1999, PASP, 111, 63
Foley, R. J., Chornock, R., Filippenko, A. V., et al. 2009, AJ, 138, 376
Foley, R. J., Rest, A., Stritzinger, M., et al. 2010, AJ, 140, 1321
Foley, R. J., Challis, P., Chornock, R., et al. 2013, ApJ, 767, 57
Fransson, C., Houck, J., Kozma, C. 1994, Stockholm Observatory/Sweden, 32
Friesen, B., Baron, E., Wisniewski, J. P., et al. 2014, ApJ, 792, 120
Gamezo, V. N., Khokhlov, A. M.,Oran, E. S., et al. 2003, Science, 299, 77
Gamezo, V. N., Khokhlov, A. M., & Oran, E. S. 2005, ApJ, 623, 337
Gerardy, C. L., Hoeflich, P., Fesen, R. A., et al. 2004, ApJ, 607, 391
Gerardy, C. L., Meikle, W. P. S., Kotak, R., et al. 2007, ApJ, 661, 995
Goldhaber, G., & Perlmutter, S. 1998, Phys. Rep., 307, 325
Hamuy, M., Phillips, M. M., Suntzeff, N. B., et al. 1996, AJ, 112, 2438
Hamuy, M., Folatelli, G., Morrell, N., et al. 2006, PASP, 118, 2
Hillier D.J. 2003, Stellar Atmosphere Modeling, eds. I. Hubeny, D. Mihalas, & K. Werner, ASP Conf. Ser., 288, 199
Hoeflich, P. 1990, A&A, 229, 191
Hoeflich, P. 2003, in Stellar Atmosphere Modeling, eds. I. Hubeny, D. Mihalas, & K. Werner, ASP Conf. Ser., 288, 185
Hoeflich, P. 2009a, in Recent Directions In Astrophysical Quantitative Spectroscopy And Radiation Hydrodynamics, eds. I. Hubeny, J. M. Stone, K. MacGregor, & K. Werner (New York: American Inst. of Physics)
Hoeflich, P. 2009b, in AIP Conf. Ser. 1171, eds. I. Hubeny, J. M. Stone, K. MacGregor, & K. Werner, 161
Hoeflich, P., & Khokhlov, A. 1996, ApJ, 457, 500
Hoeflich, P., Mueller, E., & Khokhlov, A. 1991, A&A, 248, L7
Hoeflich, P., Khokhlov, A., & Mueller, E. 1992, A&A, 259, 549
Hoeflich, P., Mueller, E., & Khokhlov, A. 1993, A&A, 268, 570
Hoeflich, P., Khokhlov, A. M., & Wheeler, J. C. 1995, ApJ, 444, 831

Hoeflich, P., Khokhlov, A., Wheeler, J.C., et al. 1996 ApJ, 472, L81

Hoeflich, P., Gerardy, C. L., Fesen, R. A., Sakai, S. 2002, ApJ, 568, 791

Hoeflich, P., Gerardy, C., Nomoto, K., et al. 2004, ApJ, 617, 1258

Hoeflich, P., Gerardy, C. L., Marion, H., & Quimby, R. 2006, New Astron. Rev., 50, 470

Hoeflich, P., Dragulin, P., Mitchell, J., et al. 2013, Frontiers of Physics, 8, 144

Höflich, P. 2006, Nucl. Phys. A, 777, 579

Hoflich, P. 1995, ApJ, 443, 89

Hsiao, E. Y., Marion, G. H., Phillips, M. M., et al. 2013, ApJ, 766, 72

Hubeny, I., & Lanz, T. 1995, ApJ, 439, 875

Jeffery, D. J., & Branch, D. 1990, Supernovae, Jerusalem Winter School for Theoretical Physics (World Scientific Publishing Co), 149

Jha, S., Branch, D., Chornock, R., et al. 2006, AJ, 132, 189

Jordan I. V., G. C., Perets, H. B., Fisher, R. T., et al. 2012, ApJ, 761, L23

Kasen, D., Röpke, F. K., & Woosley, S. E. 2009, Nature, 460, 869

Kelson, D. D. 2003, PASP, 115, 688

Khokhlov, A. M. 1991, A&A, 245, L25

Khokhlov, A. M. 1995, ApJ, 449, 695

Khokhlov, A. 2001, APS Meeting Abstracts, 3003

Khokhlov, A., Mueller, E., & Hoeflich, P. 1992, A&A, 253, L9

Khokhlov, A. M., Mueller, E., & Hoeflich, P. 1993, A&A, 270, 223

Komatsu, E., Dunkley, J., Nolta, M. R., et al. ApJS, 180, 330

Kozma, C., Fransson, C., Hillebrandt, W., et al. 2005, A&A, 437, 983

Kromer, M., Fink, M., Stanishev, V., et al. 2013, MNRAS, 429, 2287

Kurucz, R. 1994, Atomic Data for Ca, Sc, Ti, V, and Cr. Kurucz CD-ROM No. 20 (Cambridge, Mass.: Smithsonian Astrophysical Observatory), 20

Landolt, A. U. 1992, AJ, 104, 340

Leloudas, G., Stritzinger, M. D., Sollerman, J., et al. 2009, A&A, 505, L265

Lentz, E. J., Baron, E., Branch, D., Hauschildt, P. H., Nugent, P. E. 2000, ApJ, 530, 966

Li, W., Filippenko, A. V., Chornock, R., et al. 2003, PASP, 115, L453

Li W., Leaman, J., Chornock, R., et al. 2011, MNRAS, 412, 1441

Liu, W., Jeffery, D. J., & Schultz, D. R. 1997, ApJ, 483, L107

Livio, M. 1989, NATO ASIC Proc. 290: Theory of Accretion Disks (Dordrecht: Kluwer), 135

Livne, E. 1993, ApJ, 406, L17

Livne, E. 1999, ApJ, 527, L97

Livne, E., & Arnett, D. 1993, ApJ, 415, L107

Livne, E., Asida, S. M., & Hoeflich, P. 2005, ApJ, 632, L443

Lorén-Aguilar, L., Isern, J., & García-Berro, E. 2009, A&A, 500, 1193

Maeda, K., Mazzali, P. A., Deng, J., et al. 2003, ApJ, 593, 931

Maeda, K., Benetti, S., Stritzinger, M., et al. 2010, Nature, 466, 82

Maeda, K., Leloudas, G., Taubenberger, S., et al. 2011, MNRAS, 413, 3075

Maund, J., Wheeler, J.-C., Wang, L., et al. 2010, ApJ, 722, 1162

Mazzali, P., Cappellaro, E., Danziger, I., et al. 1998, MNRAS, 499, L49

McClelland, C. M., Garnavich, P. M., Galbany, L., et al. 2010, ApJ, 720, 704

McCully, C., Jha, S. W., Foley, R. J., et al. 2014a, ApJ, 786, 134

McCully, C., Jha, S. W., Foley, R. J., et al. 2014b, Nature, 512, 54

Mihalas, D., & Mihalas, B. W. 1984, Foundations of Radiation Hydrodynamics (Oxford: Oxford University)

Milne, P. A., Kurfess, J. D., Kinzer, R. L., & Leising, M. D. 2002, New Astron. Rev., 46, 553

Motohara, K., Maeda, K., Gerardy, C. L., et al. 2006, ApJ, 652, 101

Mueller, E., Hoeflich, P., & Khokhlov, A. 1991, A&A, 249, L1

Narayan, G., Foley, R. J., Berger, E., et al. 2011, ApJ, 731, L11

Nomoto, K. 1982, ApJ, 253, 798

Nomoto K., Thielemann, F.-K., & Yokoi K. 1984, ApJ, 286, 644

Nugent, P., Branch, D., Baron, E., et al. 1995a, Phys. Rev. Lett., 75, 394

Nugent, P., Phillips, M., Baron, E., Branch, D., & Hauschildt, P. 1995b, ApJ, 455, L147

Nugent, P., Baron, E., Branch, D., et al. 1997, ApJ, 485, 812

Owocki, S. P., & Cohen, D. H. 2001, ApJ, 559, 1108

Pakmor, R., Hachinger, S., Röpke, F. K., et al. 2011, A&A, 528, A117

Patat, F.,Hoeflich, P., Baade, D., et al. 2012, A&A, 545, A7

Penney, R. B. 2011, Ph.D. Thesis, The Flordia State University

Penney, R. B., & Hoeflich, P. 2014, ApJ, 795, 84

Persson, S. E., Murphy, D. C., Krzeminski, W., Roth, M., & Rieke, M. J. 1998, AJ, 116, 2475

Phillips, M. M. 1993, ApJ, 413, L105

Phillips, M. M., Lira, P., Suntzeff, N. B., et al. 1999, AJ, 118, 1766

Phillips, M. M., Li, W. D., Frieman, J. A., et al. 2007, PASP, 119, 360

Phillips, M. M., Simon, J. D., Morrell, N., et al. 2013, ApJ, 779, 38

Piersanti, L., Gagliardi, S., Iben, I., Jr., & Tornambé, A. 2003, ApJ, 598, 1229

Pinto, P. A., & Eastman, R. G. 2001, New Astron., 6, 307

Poznanski, D., Prochaska, J. X., & Bloom, J. S. 2012, MNRAS, 426, 1465

Quimby, R., Hoeflch, P., & Wheeler, J.-C. 2007, ApJ, 666, 1083

Reinecke, M., Hillebrandt, W., & Niemeyer, J. C. 2002, A&A, 391, 1167

Riess, A. G., Macri, L., Li, W., et al. 2009, ApJS, 183, 109

Riess, A. G., Macri, L., Casertano, S., et al. 2011, ApJ, 730, 119

F. K. Röpke, F. K., Woosley, S. E., & Hillebrandt, W. 2007, ApJ, 660, 1344

Roming, P. W. A., Kennedy, T. E., Mason, K. O., et al. 2005, Space Sci. Rev., 120, 95

Ruiter, A. J., Belczynski, K., Sim, S. A., Seitenzahl, I. R., & Kwiatkowski, D. 2014, MNRAS, 440, L101

Sadler, B. Hoeflich, P., Baron, E. et al. 2012, in IAU Symp. 281, eds. R. Di Stephano, & M. Orio, 309

Sahu, D. K., Tanaka, M., Anupama, G. C., et al. 2008, ApJ, 680, 592

Schlafly, E. F., & Finkbeiner, D. P. 2011, ApJ, 737, 103

Schweitzer, A., Hauschildt, P. H., & Baron, E. 2000, ApJ, 541, 1004

Seaton, M. J. 2005, MNRAS, 362, L1

Seitenzahl, I. R., Meakin, C. A., Lamb, D. Q., & Truran, J. W. 2009, ApJ, 700, 642

Seitenzahl, I. R., Ciaraldi-Schoolmann, F., Röpke, F. K., et al. 2013, MNRAS, 429, 1156

Shen, K. J., Kasen, D., Weinberg, N. N., Bildsten, L., & Scannapieco, E. 2010, ApJ, 715, 767

Silverman, J. M., Ganeshalingam, M., & Filippenko, A. V. 2013, MNRAS, 430, 1030

Sim, S. A., Fink, M., Kromer, M., et al. 2012, MNRAS, 420, 3003

Simon, J. D., Frebel, A., McWilliam, A., et al. 2010, ApJ, 715, L446

Smartt, S., Valenti, S., Fraser, M., et al. 2013, The Messenger, 154, 50

Smith, J. A., Tucker, D., Kent, S., et al. 2002, AJ, 123, 2121

Sollerman, J., Lindahl, J., Kozma, C., et al. 2004, A&A, 428, 555

Spyromilio, J., Meikle, W. P. S., Allen, D. A., & Graham, J. R. 1992, MNRAS, 258, 53

Stone, J. M., Mihalas, D., & Norman, M. L. 1992, ApJS, 80, 819

Stritzinger, M., & Sollerman, J. 2007, A&A, 470, L1

Stritzinger, M., Mazzali, P., Phillips, M. M., et al. 2009, ApJ, 696, 713

Stritzinger, M., Phillips, M. M., Boldt, L., et al. 2011, AJ, 142, 156

Stritzinger, M. D., Hsiao, E., Valenti, S., et al. 2014, A&A, 561, A146

Turatto, M., Benetti, S., Cappellaro, E., et al. 1996, MNRAS, 283, 1

Umeda, H.,Nomoto, K., Kobayashi, C., et al. 1999, ApJ, 522, L43

Valenti, S., Benetti, S., Cappellaro, E., et al. 2008, MNRAS, 383, 1485

Valenti, S., Pastorello, A., Cappellaro, E., et al. 2009, Nature, 459, 674

Wang, B., Justham, S., & Han, Z. 2013, A&A, 559, A94

White, C. J., Kasliwal, M. M., Nugent, P. E., et al. 2014, ApJ, submitted [arXiv:1405.7409]

Woosley, S. E., & Weaver, T. A. 1994, ApJ, 423, 371

Woosley, S. E., Weaver, T. A., & Taam, R. E. 1980, Texas Workshop on Type I Supernovae, 96

Yamaoka, H., Nomoto, K., Shigeyama, T., & Thielemann, F. 1992, ApJ, 393, L55

M. D. Stritzinger et al.: The bright and energetic Type Iax SN 2012Z.

Table 1. UVOT Ultraviolet photometry of SN 2012Z.

JD–2 450 000	Phase[a]	*uvw2*	*uvm2*	*uvw1*
5959.77	−8.12	17.217(122)	17.001(091)	15.853(075)
5961.95	−5.94	17.257(114)	17.191(093)	15.802(070)
5965.02	−2.87	17.371(116)	17.435(096)	15.892(082)
5967.00	−0.89	17.567(118)	17.811(102)	16.241(091)
5968.66	0.77	17.683(118)	17.855(103)	16.362(087)
5971.11	3.22	⋯	⋯	17.296(104)
5976.96	9.07	⋯	19.565(296)	⋯
5977.72	9.83	19.073(226)	⋯	17.663(107)
5979.60	11.71	19.128(230)	⋯	18.034(137)
5982.36	14.47	19.600(376)	⋯	18.093(171)
5989.79	21.90	⋯	⋯	19.094(219)
5992.13	24.24	⋯	⋯	19.341(262)
5994.01	26.12	⋯	⋯	19.483(290)
5998.08	30.19	⋯	⋯	19.532(302)

Notes. One sigma uncertainties given in parentheses are in millimag. [a] Days past $T(B)_{max}$, i.e. JD–2 455 967.89.

Table 2. Optical and NIR photometry of the local sequence of SN 2012Z in the *natural* system.

STAR	α (2000)	δ (2000)	u (mag)	N	g (mag)	N	r (mag)	N	i (mag)	N	B (mag)	N	V (mag)	N	Y (mag)	N	J (mag)	N	H (mag)	N
001	03:22:15.58	−15:19:11.93	15.026(007)	17	...	...	...	...	...	...	13.339(005)	7	...	...	...	...	...	...	...	...
002	03:22:19.50	−15:19:19.63	14.038(006)	18	...	...	...	...	...	...	13.282(005)	7	12.762(011)	1	...	...	...	...	...	...
003	03:22:00.97	−15:19:28.24	14.358(006)	18	...	...	...	...	...	...	13.399(005)	8	12.759(011)	1	...	...	...	...	...	...
004	03:21:52.18	−15:20:52.44	17.045(010)	19	16.002(003)	22	15.636(003)	20	15.501(003)	25	16.304(003)	26	15.791(003)	28	...	...	...	...	...	...
005	03:22:05.62	−15:22:34.86	17.007(010)	19	16.022(003)	22	15.618(003)	20	15.471(003)	25	16.330(003)	27	15.795(003)	29	...	...	...	...	...	...
006	03:21:54.34	−15:21:12.06	17.220(011)	19	16.101(003)	22	15.648(003)	20	15.477(003)	25	16.435(003)	27	15.849(003)	29	...	...	...	...	...	...
007	03:22:18.71	−15:19:27.70	19.076(044)	10	16.957(004)	19	16.159(004)	17	15.844(004)	20	17.441(007)	22	16.565(004)	23	...	...	...	...	...	...
008	03:22:09.62	−15:22:13.87	18.311(020)	18	17.188(004)	22	16.780(005)	20	16.616(005)	25	17.532(006)	27	16.965(004)	29	...	...	...	...	...	...
009	03:22:18.09	−15:24:01.51	...	...	18.486(010)	22	17.342(006)	20	16.861(006)	20	18.905(018)	20	17.920(008)	29	...	...	...	...	...	...
010	03:21:53.30	−15:27:14.29	...	...	19.155(024)	11	17.840(012)	12	16.165(006)	15	19.778(071)	5	18.510(018)	17	...	...	...	...	...	...
011	03:22:12.29	−15:19:41.63	...	...	19.133(019)	17	17.742(009)	18	16.700(005)	18	19.788(047)	9	18.442(013)	28	...	...	...	...	...	...
012	03:22:16.89	−15:20:44.88	18.917(082)	1	18.880(014)	21	18.060(011)	20	17.628(010)	25	18.962(024)	14	18.463(014)	29	...	...	...	...	...	...
013	03:21:48.55	−15:21:14.36	19.452(094)	3	18.817(018)	13	18.476(019)	14	18.291(023)	16	18.755(022)	14	18.587(017)	22	...	...	...	...	...	...
014	03:21:52.45	−15:27:02.48	18.958(048)	7	18.991(017)	16	18.666(019)	17	18.674(031)	18	18.970(025)	13	18.881(023)	20	...	...	...	...	...	...
015	03:22:22.44	−15:20:44.09	...	...	19.444(024)	...	18.628(017)	16	18.263(018)	19	19.445(044)	8	18.885(022)	20	...	...	...	...	...	...
016	03:21:55.41	−15:20:24.11	...	...	20.111(044)	...	18.848(021)	12	17.568(010)	19	20.147(104)	3	19.480(036)	15	...	...	...	...	...	...
017	03:22:14.78	−15:27:04.36	...	...	20.372(097)	3	19.082(032)	3	18.222(020)	11	...	...	19.656(059)	7	...	...	...	...	...	...
018	03:22:05.60	−15:22:35.06	...	...	...	...	...	...	...	...	...	...	...	...	14.808(016)	4	14.572(017)	5	14.246(014)	5
019	03:22:03.04	−15:22:27.83	...	...	...	...	...	...	...	...	...	...	...	...	16.431(024)	4	16.035(028)	5	15.384(023)	5
020	03:22:09.59	−15:22:13.71	...	...	...	...	...	...	...	...	...	...	...	...	15.973(020)	4	15.708(024)	5	15.398(022)	5
021	03:22:04.73	−15:23:44.15	...	...	...	...	...	...	...	...	...	...	...	...	16.357(033)	4	15.901(032)	5	15.245(029)	5
022	03:22:01.66	−15:22:30.86	...	...	...	...	...	...	...	...	...	...	...	...	18.399(096)	2	...	...	...	...
023	03:22:05.94	−15:24:38.59	...	...	...	...	...	...	...	...	...	...	...	...	17.229(100)	1	16.854(104)	1	16.383(119)	1

Notes. Uncertainties given in parentheses in thousandths of a magnitude correspond to an rms of the magnitudes obtained on photometric nights.

Table 3. Swope optical photometry of SN 2012Z in the *natural* system.

JD−2 450 000+	u (mag)	g (mag)	r (mag)	i (mag)	B (mag)	V (mag)
5959.57	15.631(011)	15.533(004)	15.582(005)	15.753(008)	15.591(008)	15.676(007)
5960.57	15.448(008)	· · ·	15.322(009)	15.488(009)	15.368(009)	15.416(009)
5961.57	15.323(006)	15.106(004)	15.124(005)	15.282(005)	15.171(008)	15.214(008)
5962.56	15.233(007)	· · ·	· · ·	15.115(005)	15.027(006)	15.028(005)
5963.58	15.190(011)	14.839(004)	14.814(004)	14.985(004)	14.925(007)	14.896(004)
5964.60	· · ·	14.746(006)	14.704(006)	14.871(008)	14.857(006)	14.785(005)
5965.61	15.165(016)	14.697(006)	14.608(008)	14.783(008)	14.812(009)	14.698(007)
5966.59	15.156(013)	· · ·	· · ·	14.698(006)	14.759(006)	14.619(005)
5967.59	15.199(012)	· · ·	14.472(006)	14.623(007)	14.750(007)	14.562(005)
5968.59	15.254(008)	14.584(007)	14.417(006)	14.578(008)	14.753(004)	14.512(006)
5969.59	15.321(009)	14.572(004)	14.369(004)	14.517(008)	14.780(004)	14.479(007)
5970.56	15.425(009)	14.579(004)	14.336(005)	14.467(007)	14.830(008)	14.458(008)
5971.57	15.520(010)	14.586(007)	14.288(009)	14.431(009)	14.829(006)	14.412(006)
5972.57	15.629(009)	14.646(004)	14.287(005)	14.423(008)	14.915(004)	14.422(006)
5973.55	15.751(009)	14.698(004)	14.279(004)	14.389(005)	15.007(005)	14.428(006)
5974.57	15.893(007)	14.750(004)	14.268(004)	14.370(004)	15.086(004)	14.437(004)
5979.58	16.859(009)	15.235(005)	14.322(005)	· · ·	15.699(007)	14.671(006)
5985.54	17.998(015)	15.934(004)	14.604(004)	14.470(004)	16.498(006)	15.121(005)
5986.57	18.138(017)	16.063(008)	· · ·	14.517(004)	16.601(007)	15.204(005)
5988.57	18.350(024)	16.211(005)	14.800(004)	14.608(004)	16.792(007)	15.364(005)
5990.58	18.496(051)	16.352(006)	14.925(005)	14.716(005)	· · ·	· · ·
5991.58	18.672(076)	16.422(008)	14.983(005)	14.769(004)	17.018(011)	15.559(004)
5992.56	18.656(041)	16.511(006)	15.047(008)	14.811(006)	17.074(011)	15.643(008)
5993.53	· · ·	16.562(006)	15.100(004)	14.875(004)	17.129(009)	15.694(005)
5994.54	18.764(067)	16.599(007)	15.157(004)	14.922(006)	17.168(011)	15.749(006)
5995.54	18.880(064)	16.668(008)	15.215(006)	14.969(007)	17.237(010)	15.797(007)
5996.53	18.945(038)	16.713(009)	15.267(008)	15.023(008)	17.250(014)	15.848(006)
5997.52	19.017(023)	16.743(007)	15.310(007)	15.072(008)	17.299(009)	15.890(006)
5998.52	19.063(030)	16.773(004)	15.349(004)	15.101(004)	17.347(009)	15.923(006)
5999.52	19.024(021)	16.819(011)	15.396(009)	15.168(010)	17.375(010)	15.994(009)
6000.56	· · ·	16.826(008)	15.418(004)	15.172(006)	17.395(008)	15.995(004)
6001.55	· · ·	16.847(005)	15.467(004)	15.214(005)	17.419(009)	16.024(007)
6002.55	· · ·	16.853(005)	15.502(004)	15.252(006)	17.422(009)	16.045(006)
6003.55	· · ·	16.877(005)	15.530(004)	15.275(004)	17.451(009)	16.085(004)
6004.55	· · ·	16.912(006)	15.563(004)	15.316(004)	17.474(009)	16.103(004)
6005.55	· · ·	· · ·	· · ·	15.341(004)	17.478(009)	16.121(005)
6006.54	· · ·	16.954(008)	15.623(006)	15.385(008)	17.520(009)	16.157(006)
6007.52	· · ·	16.975(009)	15.676(009)	15.404(009)	17.522(009)	16.188(009)
6009.52	· · ·	16.978(006)	15.702(006)	15.452(006)	17.545(007)	16.213(006)
6010.51	· · ·	17.000(007)	15.741(006)	15.498(008)	17.551(008)	16.235(007)
6011.52	· · ·	· · ·	· · ·	· · ·	17.596(010)	16.253(007)
6012.53	· · ·	· · ·	· · ·	· · ·	17.581(009)	16.273(005)
6014.51	· · ·	17.056(007)	15.850(005)	15.606(005)	· · ·	· · ·
6015.53	· · ·	· · ·	· · ·	· · ·	· · ·	16.335(008)
6017.52	· · ·	· · ·	· · ·	· · ·	17.625(015)	16.358(007)
6018.49	· · ·	17.097(010)	15.942(004)	15.714(004)	· · ·	· · ·
6019.49	· · ·	· · ·	· · ·	· · ·	17.644(014)	16.386(008)
6233.82	· · ·	· · ·	· · ·	20.381(119)	21.411(318)	20.876(206)

Notes. Values in parentheses are 1σ measurement uncertainties in millimag.

Table 4. du Pont NIR photometry of SN 2012Z in the *natural* system.

JD−2 450 000+	Y (mag)	J (mag)	H (mag)
5992.51541	13.899(013)	14.208(013)	13.963(012)
5996.52808	· · ·	· · ·	14.119(011)
5997.49164	14.047(012)	14.402(013)	· · ·
6000.49606	14.139(012)	14.557(013)	14.288(011)
6001.49526	14.185(013)	14.565(013)	14.277(011)
6022.46819	14.912(011)	· · ·	· · ·
6167.85063	19.818(055)	19.269(046)	· · ·
6168.82954	· · ·	19.160(065)	· · ·

Notes. Values in parentheses are 1σ measurement uncertainties in millimag.

Table 5. Journal of spectroscopic observations.

Date	JD−2 450 000+	Phase[a]	Telescope	Instrument
Optical				
2012 Feb. 01.2	5958.7	−9.2	Lick	Kast
2012 Feb. 02.2	5959.7	−8.2	Lick	Kast
2012 Feb. 04.1	5961.5	−6.4	*Clay*	MIKE
2012 Feb. 12.2	5969.7	+1.8	NOT	Alfosc
2012 Feb. 16.1	5973.6	+5.7	FLWO	FAST
2012 Feb. 18.9	5976.4	+8.5	NOT	Alfosc
2012 Feb. 19.1	5976.6	+8.7	FLWO	FAST
2012 Feb. 21.1	5978.6	+10.8	FLWO	FAST
2012 Feb. 21.3	5978.8	+11.0	Keck	LRIS
2012 Feb. 22.1	5979.6	+11.8	*Clay*	LDSS3
2012 Feb. 25.8	5983.4	+15.5	NOT	Alfosc
2012 Mar. 02.1	5988.6	+20.7	*Clay*	LDSS3
2012 Mar. 15.2	6001.7	+33.8	Keck	LRIS
2012 Aug. 22.1	6161.6	+193.7	SALT	RSS
2012 Sep. 12.3	6182.8	+214.9	du Pont	WFCCD
2012 Oct. 15.5	6216.0	+248.1	Keck	DEIMOS
NIR				
2012 Feb. 03.0	5960.6	−7.3	*Baade*	Fire
2012 Feb. 10.0	5967.5	−0.4	*Baade*	Fire
2012 Feb. 15.0	5972.5	+4.6	NTT	Sofi
2012 Feb. 21.0	5978.5	+10.6	VLT	ISAAC
2012 Feb. 27.0	5984.5	+16.6	VLT	ISAAC
2012 Mar. 03.0	5989.5	+21.6	*Baade*	Fire
2012 Mar. 14.9	6001.5	+33.6	VLT	ISAAC
2012 Mar. 29.9	6016.5	+48.6	VLT	ISAAC
2012 Apr. 07.9	6025.5	+57.6	*Baade*	Fire
2012 Nov. 05.2	6236.7	+268.8	*Baade*	Fire

Notes. [a] Days since $T(B)_{max}$, i.e., JD−2 455 967.8.

Appendix A: Definitive photometry of SN 2005hk

A portion of the CSP photometry of SN 2005hk originally published by Phillips et al. (2007) was computed from science images which underwent template subtraction using provisional template images. We returned to the field of UGC 272 and obtained updated optical *BV*- and NIR *YJHK*$_s$-band images. These were used to compute proper template subtraction for the respective science images. In addition, the field of local sequence stars was also re-calibrated based on a larger number of nights in which standard star fields were observed. Table A.1 contains the re-calibration of our optical and NIR local sequences, while our revised optical and NIR photometry of SN 2005hk is presented in Tables A.2 and A.3, respectively. We note that all of our photometry of the local sequence stars and the SN are presented in the *natural* system (Stritzinger et al. 2011).

Table A.1. Optical and NIR photometry of the local sequence of SN 2005hk in the *natural* system.

Star	α (2000)	δ (2000)	u (mag)	N	g (mag)	N	r (mag)	N	i (mag)	N	B (mag)	N	V (mag)	N	Y (mag)	N	J (mag)	N	H (mag)	N	Ks (mag)	N
001	00:27:58.40	−01:13:12.19	15.556(019)	5	14.458(009)	2	14.499(007)	3	14.590(006)	4	14.602(006)	5	14.441(006)	4	12.692(008)	5	12.480(007)	5	12.157(007)	5	⋯	⋯
002	00:27:59.34	−01:09:36.38	16.625(023)	5	15.020(007)	3	14.420(009)	2	14.201(010)	1	15.422(006)	5	14.673(006)	4	13.467(009)	4	13.226(008)	5	12.848(008)	5	⋯	⋯
003	00:28:01.15	−01:11:29.09	17.883(037)	4	16.459(006)	5	15.820(006)	5	15.582(006)	5	16.858(009)	5	16.090(008)	5	14.824(010)	5	14.530(008)	5	14.114(009)	5	⋯	⋯
004	00:28:02.93	−01:11:23.56	19.259(164)	1	17.086(007)	5	15.859(006)	5	15.355(006)	5	17.663(014)	5	16.462(009)	5	14.344(009)	5	13.970(007)	5	13.394(007)	5	⋯	⋯
005	00:27:38.83	−01:09:16.30	17.641(036)	4	16.521(006)	5	15.953(007)	5	15.733(006)	5	16.879(009)	5	16.199(009)	5	⋯	⋯	⋯	⋯	⋯	⋯	⋯	⋯
006	00:27:38.38	−01:11:30.82	18.537(060)	3	16.723(006)	5	15.911(006)	5	15.575(006)	5	17.180(011)	5	16.283(009)	5	⋯	⋯	⋯	⋯	⋯	⋯	⋯	⋯
007	00:27:51.58	−01:14:36.05	17.245(027)	5	16.258(006)	5	16.057(007)	5	16.036(007)	5	16.471(008)	5	16.127(008)	5	15.497(016)	4	15.361(013)	5	15.209(019)	5	⋯	⋯
008	00:27:50.88	−01:08:02.40	17.669(032)	4	16.706(006)	5	16.334(007)	5	16.165(007)	5	17.009(010)	5	16.467(009)	5	15.543(017)	4	15.347(017)	5	15.007(022)	5	⋯	⋯
009	00:28:00.54	−01:15:50.50	⋯	⋯	17.609(009)	4	16.492(008)	4	16.052(008)	4	18.175(019)	4	17.058(012)	4	15.092(015)	4	14.722(012)	5	14.123(013)	5	⋯	⋯
010	00:27:47.46	−01:07:55.83	18.483(057)	3	17.288(007)	5	16.685(008)	5	16.452(009)	5	17.696(014)	5	16.949(011)	5	15.651(018)	4	15.417(017)	5	15.060(023)	5	⋯	⋯
011	00:27:47.82	−01:13:59.88	19.505(198)	1	17.683(009)	5	16.823(008)	5	16.469(009)	5	18.109(018)	5	17.238(012)	5	15.624(013)	5	15.357(010)	6	14.836(014)	6	14.652(056)	1
012	00:28:02.72	−01:08:07.84	19.271(116)	2	17.845(010)	5	17.009(009)	5	16.686(010)	5	18.332(022)	5	17.448(014)	5	15.821(020)	5	15.553(019)	5	14.982(022)	5	⋯	⋯
013	00:28:12.40	−01:12:13.40	18.957(082)	3	17.640(009)	5	17.019(009)	5	16.737(010)	5	18.031(017)	5	17.298(013)	5	15.910(015)	5	15.656(014)	5	15.212(019)	5	⋯	⋯
014	00:28:05.55	−01:14:45.17	18.346(049)	3	17.413(008)	5	17.031(009)	5	16.895(011)	5	17.727(014)	5	17.194(012)	5	16.244(024)	4	16.005(023)	5	15.787(035)	5	⋯	⋯
015	00:27:41.73	−01:10:57.01	19.363(187)	1	17.871(010)	5	17.221(010)	5	16.951(012)	5	18.263(021)	5	17.511(014)	5	⋯	0	⋯	⋯	⋯	⋯	⋯	⋯
016	00:28:05.45	−01:12:24.64	⋯	⋯	18.848(022)	4	17.466(012)	4	16.602(010)	5	19.437(055)	3	18.109(022)	3	15.400(012)	5	14.998(010)	5	14.408(011)	5	⋯	⋯
017	00:27:47.99	−01:12:55.62	⋯	⋯	18.556(016)	5	17.719(014)	5	17.356(015)	5	19.006(037)	3	18.116(020)	3	16.467(023)	5	16.170(017)	6	15.545(023)	6	16.200(163)	1
018	00:27:38.35	−01:09:00.28	⋯	⋯	18.886(022)	4	17.588(013)	4	16.130(007)	5	19.637(066)	3	18.254(023)	5	⋯	0	⋯	⋯	⋯	⋯	⋯	⋯
019	00:27:37.32	−01:10:55.99	⋯	⋯	19.093(026)	4	17.845(015)	4	17.237(014)	5	19.672(067)	3	18.313(024)	5	⋯	0	⋯	⋯	⋯	⋯	⋯	⋯
020	00:27:55.68	−01:14:38.15	18.003(053)	3	18.467(015)	5	18.104(018)	5	17.856(024)	5	18.714(029)	3	18.279(024)	5	⋯	⋯	⋯	⋯	⋯	⋯	⋯	⋯
021	00:27:50.49	−01:09:04.46	18.805(107)	1	18.844(021)	4	18.504(025)	4	18.314(035)	5	19.093(041)	4	18.658(032)	5	⋯	⋯	⋯	⋯	⋯	⋯	⋯	⋯
022	00:27:55.61	−01:07:57.62	⋯	⋯	19.220(029)	4	18.886(034)	4	18.649(050)	4	19.546(060)	3	19.099(045)	3	⋯	⋯	⋯	⋯	⋯	⋯	⋯	⋯
023	00:27:36.28	−01:11:58.38	⋯	⋯	19.911(054)	3	18.732(029)	3	17.859(025)	4	20.634(198)	1	19.533(072)	3	⋯	⋯	⋯	⋯	⋯	⋯	⋯	⋯
024	00:27:58.91	−01:15:00.70	⋯	⋯	20.097(064)	3	18.748(031)	3	17.793(022)	4	⋯	⋯	18.482(041)	4	16.614(032)	4	16.169(027)	4	15.667(033)	5	⋯	⋯
025	00:27:46.17	−01:09:55.61	⋯	⋯	20.380(093)	2	19.105(042)	2	18.224(032)	4	⋯	⋯	19.740(084)	3	⋯	⋯	⋯	⋯	⋯	⋯	⋯	⋯
026	00:27:57.20	−01:13:03.18	⋯	⋯	⋯	⋯	⋯	⋯	⋯	⋯	⋯	⋯	⋯	⋯	12.692(008)	5	12.480(007)	5	12.157(007)	5	⋯	⋯
027	00:28:04.74	−01:12:35.09	⋯	⋯	⋯	⋯	⋯	⋯	⋯	⋯	⋯	⋯	⋯	⋯	13.077(008)	5	12.848(007)	5	12.498(007)	5	⋯	⋯
028	00:28:02.42	−01:09:21.58	⋯	⋯	⋯	⋯	⋯	⋯	⋯	⋯	⋯	⋯	⋯	⋯	13.261(010)	4	12.975(008)	5	12.510(009)	5	⋯	⋯
029	00:27:47.38	−01:13:05.76	⋯	⋯	⋯	⋯	⋯	⋯	⋯	⋯	⋯	⋯	⋯	⋯	16.482(023)	5	16.063(016)	6	15.492(022)	6	15.631(116)	1
030	00:28:06.38	−01:15:11.20	⋯	⋯	⋯	⋯	⋯	⋯	⋯	⋯	⋯	⋯	⋯	⋯	16.239(024)	4	15.852(021)	5	15.343(026)	5	⋯	⋯
031	00:28:02.09	−01:08:55.42	⋯	⋯	⋯	⋯	⋯	⋯	⋯	⋯	⋯	⋯	⋯	⋯	16.850(042)	4	16.548(043)	5	16.058(057)	5	⋯	⋯
032	00:28:12.89	−01:08:33.94	⋯	⋯	⋯	⋯	⋯	⋯	⋯	⋯	⋯	⋯	⋯	⋯	15.474(017)	4	15.056(014)	5	14.456(016)	5	⋯	⋯
033	00:27:45.47	−01:10:09.93	⋯	⋯	⋯	⋯	⋯	⋯	⋯	⋯	⋯	⋯	⋯	⋯	16.803(036)	4	16.356(028)	4	15.893(049)	3	⋯	⋯
034	00:28:06.44	−01:07:07.95	⋯	⋯	⋯	⋯	⋯	⋯	⋯	⋯	⋯	⋯	⋯	⋯	15.414(020)	3	15.050(016)	4	14.467(017)	4	⋯	⋯
035	00:28:13.85	−01:09:28.74	⋯	⋯	⋯	⋯	⋯	⋯	⋯	⋯	⋯	⋯	⋯	⋯	15.082(015)	3	14.704(011)	5	14.120(012)	5	⋯	⋯
036	00:27:51.47	−01:13:23.41	⋯	⋯	⋯	⋯	⋯	⋯	⋯	⋯	⋯	⋯	⋯	⋯	17.227(043)	5	16.855(031)	6	16.338(046)	5	⋯	⋯

Notes. Uncertainties given in parentheses in thousandths of a magnitude correspond to an rms of the magnitudes obtained on photometric nights.

Table A.2. Revised CSP optical photometry of SN 2005hk in the *natural* system.

JD−2 453 000+	u (mag)	g (mag)	r (mag)	i (mag)	B (mag)	V (mag)
675.61	16.759(016)	16.759(008)	16.893(009)	17.106(012)	16.830(009)	16.857(010)
682.58	16.265(014)	15.883(004)	15.945(005)	16.170(005)	15.978(006)	15.933(006)
683.58	16.280(017)	15.828(006)	15.878(007)	16.104(009)	15.930(006)	15.871(007)
684.62	16.326(018)	15.801(008)	15.833(009)	16.064(010)	15.920(007)	15.821(007)
687.60	16.541(019)	15.804(008)	15.734(008)	15.943(010)	15.967(000)	15.727(009)
689.66	16.774(024)	15.886(009)	15.701(007)	15.885(009)	16.118(009)	15.761(008)
690.61	16.917(023)	15.958(006)	15.684(004)	15.870(005)	16.185(008)	15.759(007)
694.65	17.619(026)	16.327(006)	15.709(006)	15.779(009)	16.688(009)	15.928(008)
695.64	17.812(029)	16.446(007)	15.726(008)	15.783(008)	16.829(008)	15.976(007)
698.59	18.349(041)	16.827(005)	15.869(004)	15.846(005)	17.286(009)	16.235(006)
699.62	18.688(056)	16.964(005)	15.924(004)	15.875(006)	17.428(009)	16.319(007)
702.63	19.083(066)	17.310(007)	16.108(006)	16.005(008)	17.793(014)	16.580(008)
706.66	19.538(067)	17.650(008)	16.376(009)	16.210(009)	18.166(015)	16.884(009)
712.57	19.896(123)	17.961(012)	16.669(009)	16.495(010)	18.429(018)	17.177(011)
720.57	20.265(288)	18.134(015)	16.966(007)	16.811(009)	18.647(030)	17.468(015)
725.60	20.261(117)	18.272(011)	17.127(008)	16.982(010)	18.766(020)	17.569(012)
728.61	⋯	18.332(009)	17.202(008)	17.066(009)	18.823(022)	17.663(010)
730.62	20.394(121)	18.309(009)	17.267(007)	17.135(008)	18.797(021)	17.697(011)
736.57	20.508(071)	18.411(007)	17.396(007)	17.289(008)	18.875(015)	17.782(009)
739.57	20.373(085)	18.466(008)	17.475(007)	17.367(009)	18.933(015)	17.839(010)
745.54	⋯	18.498(016)	17.588(011)	17.500(012)	18.951(048)	17.928(019)
748.56	⋯	18.528(016)	17.657(012)	17.564(013)	19.034(067)	17.993(024)
751.55	⋯	18.572(011)	17.733(011)	17.666(014)	19.069(028)	18.031(017)
761.53	⋯	18.665(019)	17.983(010)	17.841(012)	19.194(026)	18.181(013)

Notes. Values in parentheses are 1σ measurement uncertainties in millimag.

Table A.3. Revised NIR photometry of SN 2005hk in the *natural* system.

JD−2 453 000+	Y (mag)	J (mag)	H (mag)	$K_{\rm s}$ (mag)
676.49	16.818(024)	16.780(031)	16.929(061)	⋯
677.52	16.660(021)	16.545(028)	16.759(050)	⋯
678.51	16.498(019)	16.434(027)	16.593(064)	⋯
680.52	16.294(016)	16.177(024)	16.390(058)	⋯
681.57	16.225(013)	16.167(012)	16.280(016)	16.208(054)
685.60	16.024(021)	15.963(021)	16.083(038)	⋯
688.63	⋯	15.912(020)	15.907(025)	⋯
691.60	⋯	15.908(056)	⋯	⋯
692.58	⋯	⋯	15.776(026)	⋯
696.61	15.531(016)	15.888(020)	15.654(021)	⋯
697.55	15.468(013)	15.956(025)	15.600(027)	⋯
701.57	⋯	15.910(023)	15.563(021)	⋯
705.53	15.525(015)	15.979(024)	15.644(021)	⋯
710.61	15.628(014)	16.098(022)	15.805(026)	⋯
717.59	15.855(013)	16.447(027)	16.074(042)	⋯
719.60	15.906(021)	16.582(033)	16.152(047)	⋯
722.57	15.999(015)	16.710(013)	16.258(016)	16.545(123)
723.53	16.026(020)	16.814(235)	⋯	⋯
727.56	16.182(019)	16.973(050)	16.431(059)	⋯
731.54	16.322(019)	17.166(059)	16.599(063)	⋯
743.57	16.746(015)	17.605(023)	16.976(036)	⋯
756.55	17.184(027)	17.998(052)	⋯	⋯

Notes. Values in parentheses are 1σ measurement uncertainties in millimag.